

Decision-Focused Optimal Transport

Suhan Liu

Department of Statistics and Operations Research, University of North Carolina at Chapel Hill, suhanliu@unc.edu

Mo Liu

Department of Statistics and Operations Research, University of North Carolina at Chapel Hill, mo_liu@unc.edu

We propose a fundamental metric for measuring the distance between two distributions. This metric, referred to as the decision-focused (DF) divergence, is tailored to stochastic linear optimization problems in which the objective coefficients are random and may follow two distinct distributions. Traditional metrics such as KL divergence and Wasserstein distance are not well-suited for quantifying the resulting cost discrepancy, because changes in the coefficient distribution do not necessarily change the optimizer of the underlying linear program. Instead, the impact on the objective value depends on how the two distributions are coupled (aligned). Motivated by optimal transport, we introduce decision-focused distances under several settings, including the optimistic DF distance, the robust DF distance, and their entropy-regularized variants. We establish connections between the proposed DF distance and classical distributional metrics. For the calculation of the DF distance, we develop efficient computational methods. We further derive sample complexity guarantees for estimating these distances and show that the DF distance estimation avoids the curse of dimensionality that arises in Wasserstein distance estimation. The proposed DF distance provides a foundation for a broad range of applications. As an illustrative example, we study the interpolation between two distributions. Numerical studies, including a toy newsvendor problem and a real-world medical testing dataset, demonstrate the practical value of the DF distance.

Key words: decision-focused divergence, optimal transport, interpolation, distributional coupling, stochastic optimization

1. Introduction

Measuring the distance between two probability distributions is a fundamental problem in statistics and machine learning. A well-designed distance metric is a critical tool for clustering, interpolation, kernel weighting, anomaly detection, and many other tasks. Classical choices include the *total variation* (TV) distance and the *Kullback–Leibler* (KL) divergence. In particular, given two probability measures P and Q on a measurable space (Ω, \mathcal{F}) that admit densities p and q with

respect to a common dominating measure μ , the total variation distance is defined as

$$d_{\text{TV}}(P, Q) := \sup_{A \in \mathcal{F}} |P(A) - Q(A)| = \frac{1}{2} \int_{\Omega} |p(x) - q(x)| d\mu(x).$$

The KL divergence is defined as

$$D_{\text{KL}}(P \| Q) := \int_{\Omega} \log\left(\frac{dP}{dQ}\right) dP = \int_{\Omega} p(x) \log\left(\frac{p(x)}{q(x)}\right) d\mu(x),$$

with the convention that $D_{\text{KL}}(P \| Q) = +\infty$ if P is not absolutely continuous with respect to Q .

A key limitation of TV distance and KL divergence is that they compare probability mass *at the same location*. Consequently, these metrics can become ill-behaved or uninformative under *support mismatch*. For example, if there exists a measurable set $A \in \mathcal{F}$ such that $P(A) > 0$ but $Q(A) = 0$, then $D_{\text{KL}}(P \| Q) = +\infty$, while $d_{\text{TV}}(P, Q)$ can saturate. This behavior motivates distances that incorporate the geometry of Ω .

A prominent alternative is the *Wasserstein distance*, defined via optimal transport. Suppose Ω is equipped with a norm $\|\cdot\|$ (e.g., $\Omega \subseteq \mathbb{R}^d$). For $p \geq 1$, the p -Wasserstein distance between P and Q is

$$W_p(P, Q) := \left(\inf_{\pi \in \Pi(P, Q)} \int_{\Omega \times \Omega} \|x - y\|^p d\pi(x, y) \right)^{1/p}, \quad (1)$$

where $\Pi(P, Q)$ denotes the set of all *couplings* of P and Q , i.e., probability measures on $\Omega \times \Omega$ whose marginals are P and Q . In contrast to TV distance and KL divergence, Wasserstein distances quantify *how far* probability mass must be transported to transform one distribution into the other. This geometric viewpoint naturally accommodates support mismatch and aligns with the interpretation of “transporting uncertainty”.

Beyond providing a single scalar measure of discrepancy, the optimal transport problem in (1) also returns an optimizer $\pi^* \in \Pi(P, Q)$, which reveals how probability mass under P is matched to probability mass under Q . In the special case where there exists a deterministic mapping $T : \Omega \rightarrow \Omega$

such that, if $X \sim P$ then $T(X) \sim Q$, the optimal coupling is induced by T and is often called an optimal transport map. In general, however, π^* represents a many-to-many, probabilistic correspondence between points drawn from P and points drawn from Q , and can be interpreted as a “least-cost” way to transform P into Q under the transportation cost $|x - y|^p$. This coupling viewpoint has proved useful in modeling diffusion and mixing phenomena, quantifying distributional dynamics over time, and characterizing distribution shift.

1.1. Decision-focused setting

In many operations research applications, uncertain quantities enter a downstream optimization problem as objective coefficients or constraint parameters. In such stochastic optimization problems, from the *decision-focused* settings, the goal of comparing two distributions is not purely geometric. Instead, it is to quantify how distributional changes affect the optimizer and the resulting objective value. This perspective highlights a key limitation of classical distributional metrics, including d_{TV} , D_{KL} , and W_p . These metrics quantify discrepancies between probability measures on Ω , but they do not directly reflect the fact that substantial changes in the distribution may leave the optimizer unchanged, while small geometric changes may move probability mass across decision boundaries and lead to a disproportionate decision impact.

To motivate a distance metric aligned with decision regret, we consider a medical testing example in which we aim to quantify the distance between two distributions of *bone mineral density* (BMD) across two age groups.

Preventive healthcare and diagnostic testing. Let us consider the evolution of BMD within a population, which can inform treatment planning for diseases such as osteoporosis. Suppose the hospital has empirical distributions of BMD for two demographic groups, age 40 and age 50, measured from historical cohorts. These two distributions are illustrated in the top and bottom rows of Figure 1, respectively. Suppose patients at age 40 receive a treatment plan optimized for their

current BMD value. The hospital's question is whether this plan should be maintained until age 45: given the potential evolution of BMD, is the current treatment still optimal at age 45? If not, what is the resulting suboptimality gap? This question is challenging because, when decisions are made at age 40, future measurements at age 45 for the same cohort are not available. Therefore, constructing a principled forecast for the intermediate-age distribution and evaluating its decision consequences are both critical.

Estimating the optimal treatment adjustment is nontrivial because the decision must satisfy feasibility and safety constraints (e.g., upper and lower dosage limits, total budget constraints, and drug-drug interaction constraints). Consequently, the optimal decision can change discontinuously with respect to BMD and other clinical indicators (e.g., BMI, lab results, and comorbidity scores).

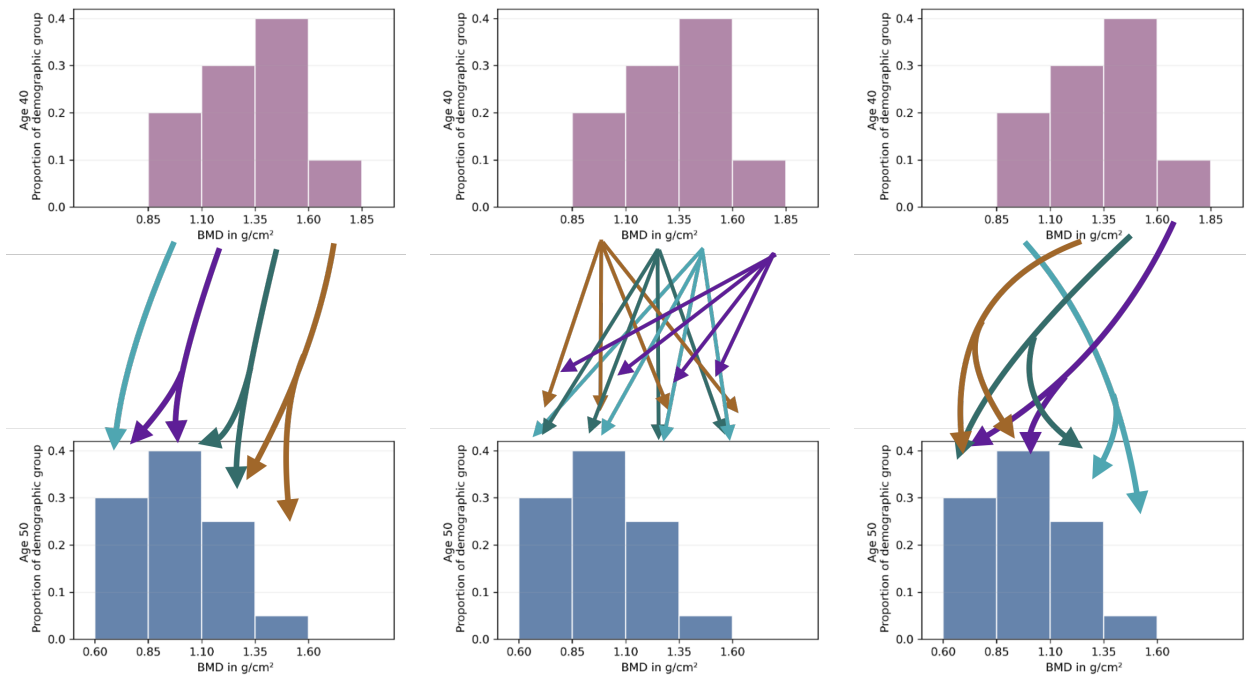
Why coupling matters. To forecast outcomes at age 45, it is not enough to specify only the marginal distributions at ages 40 and 50. The hospital must also reason about how individuals and subpopulations evolve from age 40 to age 50. This evolution is captured by a *coupling* between the two marginal distributions. Different couplings can imply very different conditional behaviors, and therefore substantially different decision risks. Given a coupling between ages 40 and 50, an interpolation (e.g., a McCann interpolation) induces a corresponding distribution at age 45.

Concretely, a coupling enables two complementary decision questions:

- **Individual level:** Conditional on a patient's observed BMD at age 40, what is a plausible distribution of this patient's features at age 45 (and age 50), and how does this affect the recommended treatment?
- **Population level:** Conditional on the age-40 BMD distribution for a subpopulation (e.g., a clinic or geographic region), what is a plausible distribution at age 45, and what is the resulting distribution of decisions and costs?

Three interpolations via couplings. Figure 1 visualizes three representative couplings between the age-40 and age-50 BMD distributions. Each coupling implies a different set of predicted patient trajectories and can induce substantially different decision outcomes. In Figure 1a, each individual’s BMD is shifted by the smallest amount necessary to match the two marginals; consequently, if the age-40 treatment is maintained, the implied decision risk is relatively small. In contrast, Figure 1c depicts an alignment that maximizes transport, suggesting that the age-40 treatment is likely to be suboptimal at age 50, and that a new BMD test and treatment adjustment may be needed. Figure 1b represents an “independent” scenario, where the age-50 BMD distribution is the same for all individuals, regardless of their BMD at age 40. In real-world settings, as shown in Section 6.2, Figure 1a most closely reflects the true dynamics, whereas the independent case in Figure 1b can overestimate the average decision loss.

Beyond summarizing population shift, the couplings in Figure 1 also induce patient-level conditional forecasts. Figure 2 illustrates this effect for a representative patient with $BMD = 1.7$ at age 40. Under an optimistic coupling, the patient is matched to the closest BMD outcome at age 50; under an independent coupling, the patient’s BMD evolves toward the marginal age-50 distribution without individual-level persistence; under a robust coupling, the patient is matched to the farthest BMD outcome. These patient-level differences can translate into distinct downstream actions and costs, even though the marginal distributions at ages 40 and 50 are identical across the three scenarios.



(a) Optimistic coupling (best-case alignment). (b) Independent coupling (no persistence). (c) Robust coupling (worst-case alignment).

Figure 1 Three couplings between age 40 and age 50 BMD distributions. The arrows illustrate how probability mass at age 40 is matched to mass at age 50. Different couplings lead to different conditional trajectories and can induce substantially different decision risks. Figure 1a corresponds to a minimal-change alignment (small individual-level shifts), Figure 1c corresponds to a maximal-change alignment (large individual-level shifts), and Figure 1b corresponds to an independent scenario in which each individual shares the same age-50 target distribution, regardless of their BMD at age 40.

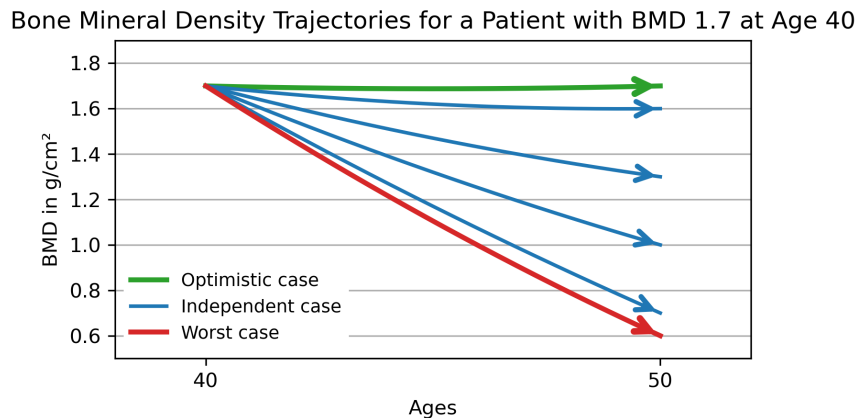


Figure 2 Patient-level trajectories implied by different coupling assumptions. The figure shows plausible BMD paths for a patient with BMD = 1.7 at age 40 under an optimistic coupling (best-case alignment), an independent coupling, and a robust coupling (worst-case alignment).

Decision-focused average at age 45. For the current age-40 cohort, suppose that the hospital must decide whether to allocate resources to measure them again at age 45 before deploying a treatment or testing policy. Decision-focused interpolation (decision-focused average between ages 40 and 50) enables a comparison of plausible intermediate risks implied by different coupling assumptions. If the risk exceeds a clinical tolerance threshold, then new measurements at age 45 are warranted. Otherwise, the hospital can justify proceeding with a policy derived from historical cohorts. This motivates the need for a decision-focused distance notion that evaluates distributional discrepancy through the lens of downstream optimization, rather than purely through geometric comparisons.

Beyond healthcare, decision-focused divergences have wide applications in *personalized recommendations, insurance pricing, inventory allocation*, and other OR problems. For example, in the newsvendor problem, as long as the critical quantile remains unchanged, many distribution shifts yield zero decision impact and should therefore correspond to a zero (or near-zero) decision-focused divergence.

Classical divergences such as d_{TV} and D_{KL} depend only on marginal distributions and compare probability mass at the same location; they do not encode how individuals transition over time. The Wasserstein distance W_p improves upon this by producing a coupling, but the coupling is selected to minimize a geometric transportation cost, which may be misaligned with the downstream decision structure. Two distributions can be far in W_p while inducing nearly identical optimizers, and conversely, a small geometric shift can have a large decision impact if it moves mass across regions with different optimal decisions. The main contributions of this paper are summarized as follows:

- We propose a new metric, termed the *decision-focused divergence*, for measuring the decision discrepancy between two distributions of objective coefficient vectors in stochastic linear optimization. We study several variants, including the optimistic DF distance, the robust DF distance, and

their entropy-regularized versions. The proposed metric provides a foundation for a broad range of future research directions, including interpolation, anomaly detection, uncertainty set construction, kernel regression, and clustering.

- We establish key theoretical properties of the DF distance, including Lipschitz-type bounds in terms of W_1 , W_2 , D_{KL} , and d_{TV} , as well as sandwich inequalities for the entropy-regularized variants. (Section 3)
- We develop efficient computational methods for evaluating the DF divergence by showing an equivalent transformation to a W_2 -type distance. (Section 4)
- While the sample complexity of estimating Wasserstein distances typically deteriorates exponentially with the dimension of distributions, we show that the proposed DF distance admits an $\mathcal{O}(1/\sqrt{n})$ estimation rate that is independent of dimension. This improvement arises because the downstream feasible region has finitely many extreme points. (Section 4.1)
- As an illustrative application, we show how the decision-focused divergence can be used to construct McCann-type interpolations between distributions. These decision-focused interpolations provide a better estimate of intermediate distributional dynamics than decision-blind alternatives (Section 5).
- We conduct numerical experiments in two settings: (i) a toy newsvendor example and (ii) a real-world Parkinson’s disease study. These experiments demonstrate the practical value of the proposed DF distance and show that traditional metrics can substantially overestimate decision risk by ignoring couplings.

Organization of the paper. In Section 2, we formally define the decision-focused divergence, including symmetric variants and entropy-regularized versions. In Section 3, we establish key properties of the proposed divergence, including its connections to d_{TV} , D_{KL} , and the Wasserstein distance W_p . Building on these results, Section 4 develops efficient computational methods for

evaluating the associated coupling, and Section 4.1 derives dimension-independent convergence rates for estimating the divergence. In Section 5, we illustrate an illustration via an interpolation problem motivated by medical testing, and Section 6 evaluates the proposed DF distance in two settings: A toy example of the newsvendor problem in Section 6.1 and real-world Parkinson’s disease treatment in Section 6.2. Finally, Section 7 concludes the paper.

1.2. Literature review

Since this work is the first to propose a distributional divergence tailored to a stochastic optimization setting, we organize the literature review around two streams: (i) decision-focused learning for stochastic optimization and (ii) distributional distance measures based on optimal transport.

Decision-focused learning for stochastic linear optimization. Decision-focused learning (also referred to as decision-aware, task-based, or end-to-end learning) is motivated by the observation that improved prediction accuracy does not necessarily lead to improved downstream decision quality in stochastic optimization. This decision-focused learning has attracted growing attention for solving stochastic optimization in recent years; see Mandi et al. (2024), Sadana et al. (2025) for comprehensive surveys. We highlight two subsets of related papers. The first subset focuses on estimating the full information of the uncertainty. Bertsimas and Kallus (2020), Elmachtoub et al. (2023, 2025) study the sample average approximation (SAA) in the decision-focused setting. Robust formulations that jointly account for estimation and optimization have been studied in, e.g., Zhu et al. (2022). Qi et al. (2025) considers estimating right-hand-side uncertainty in constraints by incorporating decision loss, and Cristian et al. (2025) addresses computational challenges by proposing training methods that approximate the optimization oracle solver. The second subset focuses on constructing point-wise predictions via decision-aligned losses. Elmachtoub and Grigas (2022) and Huang and Gupta (2024) propose surrogate loss functions and establish consistency under various conditions. Homem-de Mello et al. (2024), Er and Liu (2025) characterize the existence of decision-unbiased

predictions. Statistical guarantees and comparisons with decision-blind approaches are provided in Elmachtoub et al. (2023), El Balghiti et al. (2022), Hu et al. (2022), Liu et al. (2023).

The above literature primarily focuses on learning under a fixed distribution and does not explicitly model *distributional dynamics* in a decision-focused manner. In contrast, our work studies how distributions evolve and how such evolution should be measured through the lens of downstream linear optimization, using tools inspired by optimal transport.

Distributional distances and optimal transport. A rich set of metrics and divergences has been proposed to quantify discrepancies between probability distributions. In one dimension, CDF-based distances such as the Kolmogorov–Smirnov (KS) distance and the Cramér–von Mises (CvM) distance are widely used. In higher dimensions, when distributions share a common support, the total variation (TV) distance provides a strong notion of discrepancy. Asymmetric divergences defined via density ratios, such as the KL divergence and the chi-square (χ^2) divergence, are also standard choices under common support. In the OR community, KL-based uncertainty sets have been used in distributionally robust optimization; see, e.g., Bennouna and Van Parys (2022).

Compared with the above metrics, the Wasserstein distance has two distinguishing features: (i) it is defined through an optimal transport problem and thus induces an explicit coupling that describes how probability mass is moved from one distribution to another, and (ii) it naturally accommodates support mismatch. The Wasserstein distance has been widely used in the OR literature because, for many objective functions, their expected objective value is Lipschitz with respect to the Wasserstein distance between the underlying uncertainty distributions (e.g. Blanchet and Murthy (2019)); for an overview of methods and applications, see Kuhn et al. (2019). Using Wasserstein-based uncertainty sets, recent work has developed strong guarantees and finite-sample analysis for distributionally robust optimization; see, e.g., Blanchet et al. (2022), Ho-Nguyen et al. (2023), Gao et al. (2024), Gao (2023).

The Wasserstein distance in the above literature is inherently *decision-blind*: it captures geometric discrepancy between distributions without accounting for the structure of the downstream optimization problem. In contrast, the proposed decision-focused divergence incorporates the geometry of the feasible region of a linear program and is therefore directly aligned with decision impact. This alignment enables decision-focused clustering, interpolation, kernel regression, and other applications where the relevant notion of distributional proximity is governed by downstream decisions.

2. Decision-Focused Divergence

Let μ and ν be probability measures on \mathbb{R}^d , and let $c : \mathbb{R}^d \times \mathbb{R}^d \rightarrow [0, \infty)$ be a measurable cost function. A *coupling* of μ and ν is a probability measure γ on $\mathbb{R}^d \times \mathbb{R}^d$ whose marginals are μ and ν ; we denote the set of all such couplings by $\Gamma(\mu, \nu)$ (equivalently, $\Gamma_{\mu, \nu}$). In particular, $\gamma \in \Gamma(\mu, \nu)$ if and only if, for every bounded measurable function $f : \mathbb{R}^d \rightarrow \mathbb{R}$,

$$\int f(x) \gamma(dx, dy) = \int f d\mu \quad \text{and} \quad \int f(y) \gamma(dx, dy) = \int f d\nu.$$

The (Kantorovich) optimal transport problem seeks a coupling that minimizes the expected transport cost,

$$\inf_{\gamma \in \Gamma(\mu, \nu)} \int_{\mathbb{R}^d \times \mathbb{R}^d} c(x, y) \gamma(dx, dy). \quad (2)$$

Any $\gamma \in \Gamma(\mu, \nu)$ can be interpreted as the joint law of a pair (X, Y) with marginals $X \sim \mu$ and $Y \sim \nu$. A classical choice is the power cost $c(x, y) = \|x - y\|^p$, which leads to the W_p distance in (1). As a special case, when μ and ν have finite second moments, the corresponding optimal transport value defines the quadratic Wasserstein distance

$$W_2(\mu, \nu) = \inf_{\gamma \in \Gamma(\mu, \nu)} \left(\int_{\mathbb{R}^d \times \mathbb{R}^d} \|x - y\|_2^2 \gamma(dx, dy) \right)^{1/2}. \quad (3)$$

In decision-focused learning, the discrepancy between x and y should not be purely geometric: what matters is how much the downstream decision quality degrades if we optimize for x but face

y . To formalize this, we consider a downstream stochastic linear optimization problem. Let X and $Y \in \mathbb{R}^d$ be random cost (coefficient) vectors, and let $S \subset \mathbb{R}^d$ be a nonempty compact polyhedron representing the feasible region. When the cost vector X follows distribution μ , the downstream problem chooses $w \in S$ to minimize the expected objective $\mathbb{E}_\mu[X^\top w]$. For a realized cost vector $x \in \mathbb{R}^d$, the corresponding optimal decision is obtained by the optimization oracle $w^*(\cdot) : \mathbb{R}^d \rightarrow \mathbb{R}^d$,

$$w^*(x) \in \arg \min_{w \in S} w^\top x. \quad (4)$$

Because S is polyhedral, $w^*(\cdot)$ can be chosen to take values in the (finite) set of extreme points of S and is piecewise constant over a polyhedral partition of \mathbb{R}^d . As we show later, this piecewise-constant structure is a key property for deriving sharper estimation-error bounds for decision-focused transport.

To formally capture the decision discrepancy between two cost vectors $x, y \in \mathbb{R}^d$, we adopt the *Smart Predict-then-Optimize (SPO)* loss, defined as $\ell_{\text{SPO}}(x, y) := y^\top w^*(x) - y^\top w^*(y)$, i.e., the objective difference between the decisions of $w^*(x)$ and $w^*(y)$, when the true vector is y . The SPO loss is nonnegative and was introduced in Elmachtoub and Grigas (2022) in a contextual setting.

Using the SPO loss $\ell_{\text{SPO}}(x, y)$ as the transport cost $c(x, y)$ in (2) yields a decision-focused transport objective tailored to the downstream stochastic linear optimization problem. Since the SPO loss is generally asymmetric, i.e., $\ell_{\text{SPO}}(x, y) \neq \ell_{\text{SPO}}(y, x)$, the resulting transport-based discrepancy is also asymmetric. We therefore define it as a *divergence*.

DEFINITION 1 (DECISION-FOCUSED DIVERGENCE). Given μ, ν and a coupling $\gamma \in \Gamma(\mu, \nu)$, the *decision-focused divergence* (DF divergence) is

$$W_{\text{SPO}}(\mu, \nu; \gamma) := \int_{\mathbb{R}^d \times \mathbb{R}^d} \ell_{\text{SPO}}(x, y) \gamma(dx, dy). \quad (5)$$

The DF divergence depends on the joint law γ (not only on the marginals). In particular, if $X \sim \mu$ and $Y \sim \nu$ are independent, then $\gamma = \mu \otimes \nu$, the product (independent) coupling of μ and ν , and (5) reduces to the classical expected regret

$$R(\mu, \nu) := \mathbb{E}[\ell_{\text{SPO}}(X, Y)] = W_{\text{SPO}}(\mu, \nu; \mu \otimes \nu). \quad (6)$$

Although the regret (6) has been widely used to evaluate decision loss, the independence assumption behind $\mu \otimes \nu$ can be inappropriate when there is strong dependence between X and Y . For example, if a patient's BMD at age 40 is below average (e.g., 0.6), it is unlikely that this patient's BMD will exceed 1.6 at age 50, even if values above 1.6 are common in the overall population. In such settings, the joint distribution, i.e., the coupling between μ and ν , should be modeled carefully. Varying γ over $\Gamma(\mu, \nu)$ corresponds to varying how outcomes drawn from μ are aligned with outcomes drawn from ν , which can substantially change the average decision loss. Our numerical study on real-world data further shows that ignoring dependence can significantly overestimate decision loss in practice. This motivates the following extremal coupling-based quantities.

DEFINITION 2 (DECISION-FOCUSED DISTANCES). Given two measures μ and ν , the *optimistic* and *robust* decision-focused distances are defined by

$$W_{\text{DF}}^{\text{O}}(\mu, \nu) := \inf_{\gamma \in \Gamma(\mu, \nu)} W_{\text{SPO}}(\mu, \nu; \gamma), \quad (\text{Optimistic DF distance})$$

$$W_{\text{DF}}^{\text{R}}(\mu, \nu) := \sup_{\gamma \in \Gamma(\mu, \nu)} W_{\text{SPO}}(\mu, \nu; \gamma). \quad (\text{Robust DF distance})$$

Since $\mu \otimes \nu \in \Gamma(\mu, \nu)$, we always have $0 \leq W_{\text{DF}}^{\text{O}}(\mu, \nu) \leq R(\mu, \nu) \leq W_{\text{DF}}^{\text{R}}(\mu, \nu)$. As suggested by their names, Optimistic DF distance corresponds to the best-case (most favorable) alignment between μ and ν , while Robust DF distance corresponds to the worst-case (least favorable) alignment and thus a conservative assessment of decision risk. The distances $W_{\text{DF}}^{\text{O}}(\mu, \nu)$ and $W_{\text{DF}}^{\text{R}}(\mu, \nu)$ are generally asymmetric in (μ, ν) . This asymmetry arises because evaluating decisions derived from μ under ν

differs from evaluating decisions derived from ν under μ . In practice, we can further consider two symmetric variants: the additive symmetrization

$$W_{\text{sym}}^O(\mu, \nu) := W_{\text{DF}}^O(\mu, \nu) + W_{\text{DF}}^O(\nu, \mu), \quad W_{\text{sym}}^R(\mu, \nu) := W_{\text{DF}}^R(\mu, \nu) + W_{\text{DF}}^R(\nu, \mu),$$

and a Jensen–Shannon type symmetrization based on the midpoint mixture $m := (\mu + \nu)/2$,

$$W_{\text{JS}}^O(\mu, \nu) := \frac{1}{2}W_{\text{DF}}^O(\mu, m) + \frac{1}{2}W_{\text{DF}}^O(\nu, m), \quad W_{\text{JS}}^R(\mu, \nu) := \frac{1}{2}W_{\text{DF}}^R(\mu, m) + \frac{1}{2}W_{\text{DF}}^R(\nu, m).$$

The paper primarily focuses on the asymmetric notion in Definition 2, since the main properties extend naturally to the corresponding symmetric variants. Accordingly, we refer to Definition 2 as a *distance* rather than a divergence.

One of the motivations for Optimistic DF distance is that, in real-world settings (e.g., disease progression or market changes), traditional regret notions can lead $R(\mu, \nu)$ to substantially overestimate the average decision loss; see Section 6. In practice, μ and ν are often correlated (for instance, an individual patient’s status typically changes gradually even when the population-level distribution varies considerably). In such cases, Optimistic DF distance provides a more accurate estimate of decision loss. The motivation for Robust DF distance follows from the robust perspective in operations research decision making, which are detailed in Appendix B. To further motivate these definitions, we present a geometric example in Section 2.1.

2.1. Examples of decision-focused divergence

In this section, we illustrate the geometry underlying Optimistic/Robust DF distance in a two-dimensional setting ($d = 2$). Consider a polyhedral feasible region $S \subset \mathbb{R}^2$ with four extreme points, as shown in Fig. 3 (left). For each extreme point w_k of S , the set of cost vectors for which w_k is an optimizer of (4) is a polyhedral cone (the normal cone of S at w_k), which we denote by $C_k := \{c \in \mathbb{R}^2 : w_k \in \arg \min_{w \in S} w^\top c\}$ and label as *Cone* k . These cones form a partition of the cost

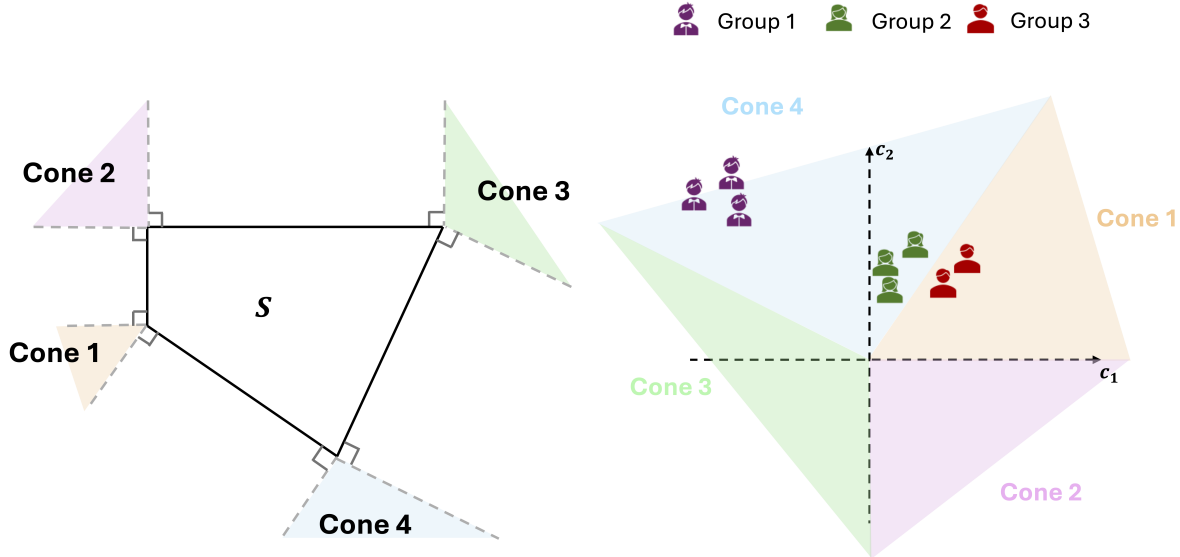


Figure 3 Left: a polyhedral feasible region S with four extreme points and their associated normal cones. Right: the point clouds illustrate three example groups of cost vectors. The DF distance between Groups 1 and 2 is zero, while the DF distance between Groups 2 and 3 is nonzero.

space (up to boundaries where multiple extreme points are optimal), as depicted in Fig. 3 (right).

In particular, the oracle map is constant on each cone: if $x \in C_k$, then $w^*(x) = w_k$.

This cone structure makes the SPO loss highly sensitive to whether x and y fall in the same cone. If x and y belong to the same cone C_k , then $w^*(x) = w^*(y)$ and hence $\ell_{\text{SPO}}(x, y) = 0$. Consequently, the decision-focused divergence (5) can be small (or even zero) when the coupling γ mostly pairs outcomes within the same cones, even if the paired points are far apart in Euclidean distance. Conversely, a small geometric perturbation that moves probability mass across a cone boundary can change the optimizer of $w^*(\cdot)$, leading to a strictly positive $\ell_{\text{SPO}}(x, y)$ despite $\|x - y\|$ being small.

The right panel of Fig. 3 provides a concrete illustration with three point clouds (Groups 1–3). Each group can represent an empirical distribution over cost vectors for different customers or patients. For example, Groups 1, 2, and 3 represent patient cohorts at ages 40, 45, and 50, respectively. Groups 1 (purple) and 2 (green) lie in Cone 4, and thus induce the same oracle decision, while Group 3 (red) lies in Cone 1 and induces a different decision. As a result, purely geometric

distances may regard Groups 2 and 3 as close, yet the induced decisions can differ; in contrast, Groups 1 and 2 may be geometrically far apart but decision-wise identical. In particular, if two measures μ and ν are supported entirely within the same cone, then $w^*(X) = w^*(Y)$ almost surely for any coupling $\gamma \in \Gamma(\mu, \nu)$, implying $W_{\text{SPO}}(\mu, \nu; \gamma) = 0$ and hence $W_{\text{DF}}^{\text{O}}(\mu, \nu) = W_{\text{DF}}^{\text{R}}(\mu, \nu) = 0$. More generally, when μ and ν place mass on multiple cones, Optimistic DF distance favors couplings that align mass *within* the same cones (to keep $w^*(X) = w^*(Y)$ as often as possible), whereas Robust DF distance corresponds to the most adverse alignment that maximizes decision degradation. This perspective clarifies why coupling choice is central in decision-focused transport, and why the optimistic and robust quantities in decision-focused distance can differ substantially.

To conclude this section of examples, we note that W_{DF}^{O} can be zero under a broad class of couplings, even when μ and ν are geometrically far apart. This occurs whenever the coupling aligns (X, Y) so that the downstream optimizer is preserved, i.e., $w^*(X) = w^*(Y)$ almost surely. A basic (and important) instance follows from the scale-invariance property $w^*(x) = w^*(cx)$ for any $c > 0$, as shown in Proposition 1.

PROPOSITION 1 (Random rescaling yields zero optimistic DF distance). *Let $X \in \mathbb{R}^d$ be any random cost vector with distribution μ . Let κ be any nonnegative random scalar (which may depend on X), and define the transformed vector $Y := \kappa X$, with distribution ν . Then we have $W_{\text{DF}}^{\text{O}}(\mu, \nu) = 0$.*

The proof of Proposition 1, along with other omitted proofs, is provided in the appendix.

2.2. Entropy-regularized DF divergences

The optimistic and robust DF divergences in Definition 2 correspond to two extreme cases: the best-case and the worst-case couplings, respectively. As a result, these estimates can be overly optimistic or overly pessimistic in practice. Moreover, extreme couplings can be brittle: small changes in empirical measures may lead to substantially different transport plans. To mitigate these issues and to define distance notions that lie between the two extremes while still capturing meaningful dependence between μ and ν , we introduce the entropy-regularized DF divergence.

Entropy regularization is a standard tool in optimal transport for improving computational tractability and stability. Even when μ and ν are replaced by empirical distributions, the optimal transport are large-scale problems over joint distributions (equivalently, transportation plans), and the optimizer need not be unique. Entropy regularization (i) biases couplings toward a simple reference distribution, (ii) smooths and stabilizes optimization over $\Gamma(\mu, \nu)$, and (iii) yields objectives that are typically easier to compute in discrete settings. In our formulation, we regularize relative to the independent coupling $\mu \otimes \nu$, so the regularization parameter ε controls the strength of dependence imposed between μ and ν , ranging from highly structured dependence (small ε) to near-independence (large ε).

DEFINITION 3 (ENTROPY-REGULARIZED DF DIVERGENCES). For $\varepsilon > 0$, define the entropy-regularized optimistic and robust DF divergences by

$$W_{\text{DF}}^{\text{ER-O}}(\mu, \nu; \varepsilon) := \inf_{\gamma \in \Gamma(\mu, \nu)} \left\{ \int \ell_{\text{SPO}}(x, y) d\gamma(x, y) + \varepsilon \text{KL}(\gamma \| \mu \otimes \nu) \right\}. \quad (\text{E-DFO})$$

$$W_{\text{DF}}^{\text{ER-R}}(\mu, \nu; \varepsilon) := \sup_{\gamma \in \Gamma(\mu, \nu)} \left\{ \int \ell_{\text{SPO}}(x, y) d\gamma(x, y) - \varepsilon \text{KL}(\gamma \| \mu \otimes \nu) \right\}, \quad (\text{E-DFR})$$

where $\text{KL}(\gamma \| \mu \otimes \nu)$ denotes the KL divergence of γ relative to the independent coupling $\mu \otimes \nu$.

Note that (E-DFO) is a minimization problem with a positive regularization term, whereas (E-DFR) is a maximization problem with a negative regularization term. In both (E-DFO) and (E-DFR), the additional regularization term therefore acts as a penalty in the optimal transport objective. As ε increases, the optimizer is increasingly encouraged to stay close to the independent coupling (i.e., γ approaches $\mu \otimes \nu$), while $\varepsilon \downarrow 0$ recovers the unregularized optimistic and robust formulations (Optimistic DF distance and Robust DF distance).

3. Properties of the Decision-Focused Divergence

We begin with a coarse stability bound that relates the (optimistic) DF distances to standard probabilistic metrics. Throughout this section, we assume that μ and ν are supported on a bounded

set $\mathcal{Y} \subset \mathbb{R}^d$. We define the diameter of the feasible region in the decision space by $D_W := \sup\{\|w - w'\|_2 : w, w' \in S\}$, and the diameter of \mathcal{Y} by $\|\mathcal{Y}\| := \sup\{\|x - y\|_2 : x, y \in \mathcal{Y}\}$.

PROPOSITION 2 (Optimistic DF distance is Lipschitz with respect to W_1 distance). *Assume that μ and ν are supported on \mathcal{Y} . Then*

$$W_{\text{DF}}^O(\mu, \nu) \leq W_{\text{sym}}^O(\mu, \nu) \leq D_W W_1(\mu, \nu) \leq D_W \|\mathcal{Y}\| d_{\text{TV}}(\mu, \nu).$$

In particular, whenever $\text{KL}(\mu\|\nu) < \infty$, Pinsker's inequality yields

$$W_{\text{sym}}^O(\mu, \nu) \leq D_W \|\mathcal{Y}\| \sqrt{\frac{1}{2} \text{KL}(\mu\|\nu)}.$$

Proposition 2 demonstrates that the optimistic DF distance is no larger than some constant times the traditional W_1 distance and d_{TV} . Thus, a smaller geometric W_1 distance and d_{TV} also implies a smaller or equal W_{DF}^O . The bound in Proposition 2 is generic: it does not exploit the piecewise-constant structure of the oracle map $w^*(\cdot)$. We next introduce an oracle-induced (push-forward) measure that captures the intrinsic geometry of the decision problem and yields sharper control.

DEFINITION 4 (PUSH-FORWARD MEASURE). Let μ be a probability measure on a measurable space $(\Omega_1, \mathcal{F}_1)$, let $(\Omega_2, \mathcal{F}_2)$ be another measurable space, and let $f : \Omega_1 \rightarrow \Omega_2$ be measurable. The push-forward of μ by f , denoted $f_{\#}\mu$, is the measure on $(\Omega_2, \mathcal{F}_2)$ defined by

$$(f_{\#}\mu)(B) := \mu(f^{-1}(B)), \quad B \in \mathcal{F}_2.$$

In our setting, we take $f = w^*$ and $\Omega_1 = \mathcal{Y} \subset \mathbb{R}^d$. Since S is polyhedral, we may choose $w^*(\cdot)$ to take values in the set of extreme points $\mathfrak{S} = \{w_1, \dots, w_{|\mathfrak{S}|}\}$. Writing $D_i := \{x \in \mathcal{Y} : w^*(x) = w_i\}$, the push-forward measure $w_{\#}^*\mu$ is the discrete distribution on \mathfrak{S} given by

$$w_{\#}^*\mu(\{w_i\}) = \mu(D_i), \quad i = 1, \dots, |\mathfrak{S}|.$$

If $X \sim \mu$, then $w^*(X)$ is a random decision supported on \mathfrak{S} and has distribution $\mathcal{L}(w^*(X)) := w_{\#}^*\mu$.

The next proposition relates $W_{\text{DF}}^{\text{O}}(\mu, \nu)$ to the quadratic Wasserstein distance between the oracle-induced measures. Intuitively, $w_{\#}^*\mu$ and $w_{\#}^*\nu$ record how μ and ν distribute mass across oracle regions (or, equivalently, across extreme-point decisions).

PROPOSITION 3 (Optimistic DF distance is Lipschitz with respect to W_2 distance). *Let $V^2 := \int_{\mathbb{R}^d} \|y\|_2^2 \nu(dy) < \infty$. Then*

$$W_{\text{DF}}^{\text{O}}(\mu, \nu) \leq V W_2(w_{\#}^*\mu, w_{\#}^*\nu).$$

Moreover,

$$W_{\text{DF}}^{\text{O}}(\mu, \nu) \leq V D_W \sqrt{d_{\text{TV}}(w_{\#}^*\mu, w_{\#}^*\nu)} \leq V D_W \left(\frac{1}{2} \text{KL}(w_{\#}^*\mu \| w_{\#}^*\nu) \right)^{1/4}.$$

Propositions 2 and 3 control the optimistic DF distance in terms of the Wasserstein distance, since the Wasserstein distance is itself defined via an optimal transport plan. For the robust DF distance, we can show that it is uniformly bounded, since the SPO loss satisfies $\ell_{\text{SPO}}(x, y) \leq \|y\|_2 \|w^*(x) - w^*(y)\|_2 \leq D_W \|y\|_2$, which yields the bound $W_{\text{DF}}^{\text{R}}(\mu, \nu) \leq D_W \int_{\mathbb{R}^d} \|y\|_2 \nu(dy)$.

We next provide basic order relations for the entropy-regularized quantities (E-DFO)–(E-DFR). These bounds formalize the idea that entropy regularization discourages extreme couplings and favors plans closer to the independent coupling $\mu \otimes \nu$.

PROPOSITION 4 (monotonicity and sandwich inequalities for entropy-regularized DF distance).

For fixed μ and ν , the map $\varepsilon \mapsto W_{\text{DF}}^{\text{ER-O}}(\mu, \nu; \varepsilon)$ is nondecreasing on $\varepsilon \geq 0$, and the map $\varepsilon \mapsto W_{\text{DF}}^{\text{ER-R}}(\mu, \nu; \varepsilon)$ is nonincreasing on $\varepsilon \geq 0$. Moreover, for any $\varepsilon \geq 0$,

$$W_{\text{DF}}^{\text{O}}(\mu, \nu) \leq W_{\text{DF}}^{\text{ER-O}}(\mu, \nu; \varepsilon) \leq R(\mu, \nu), \quad W_{\text{DF}}^{\text{R}}(\mu, \nu) \geq W_{\text{DF}}^{\text{ER-R}}(\mu, \nu; \varepsilon) \geq R(\mu, \nu),$$

where $R(\mu, \nu)$ is the independent regret defined in (6).

Proposition 4 shows that the entropy-regularized DF distances are between the optimistic/robust DF distance and the independent regret. The value of ε further controls the degree of dependence. A larger ε drives the distance closer to the independent regret. The numerical results in Section 6 further justify these insights.

4. Calculation of Decision-Focused Optimal Transport

Computing $W_{\text{DF}}^{\text{O}}(\mu, \nu)$ and $W_{\text{DF}}^{\text{R}}(\mu, \nu)$ amounts to solving an optimal transport problem with transport cost $\ell_{\text{SPO}}(x, y)$. In particular, when μ and ν are replaced by empirical measures (i.e., n_μ samples from μ and n_ν samples from ν), the optimistic and robust DF distances reduce to large-scale linear programs. The explicit LP formulation is provided in Appendix A.

However, the direct LP formulation has $n_\mu n_\nu$ decision variables and becomes prohibitive when sample sizes are moderate or large. Moreover, when one of the distributions admits a continuous density (or when $n_\mu n_\nu$ is simply too large), it is desirable to avoid solving LP directly. For the optimistic DF distance, the polyhedral structure of the downstream problem yields a substantial reduction. The key intuition is that μ enters the optimization only through an oracle-induced discrete measure, and the only coupling-dependent term can be expressed as a quadratic Wasserstein transport problem. This is formalized by Lemma 1, Theorem 1, and the lifting result in Theorem 2. For notational convenience, we define $\bar{w}^*(x) := -w^*(x)$.

LEMMA 1 (Coupling reduction via oracle push-forward). *Fix probability measures μ, ν on \mathbb{R}^d , and let $w^* : \mathbb{R}^d \rightarrow S$ be the oracle map. For any bounded measurable $h : \mathbb{R}^d \rightarrow \mathbb{R}^d$,*

$$\inf_{\gamma \in \Gamma(\mu, \nu)} \int h(y)^\top w^*(x) d\gamma(x, y) = \inf_{\bar{\gamma} \in \Gamma(w_\#^* \mu, \nu)} \int h(y)^\top w d\bar{\gamma}(w, y).$$

Lemma 1 implies that the coupling-dependent term in the SPO loss depends on μ only through the oracle-induced measure $w_\#^* \mu$.

THEOREM 1 (Quadratic OT reformulation of W_{DF}^{O}). *Assume that μ and ν have finite second moments, and let $\bar{w}^* := -w^*$. Then*

$$W_{\text{DF}}^{\text{O}}(\mu, \nu) = \frac{1}{2} \left[W_2^2((\bar{w}^*)_\# \mu, \nu) - \|w_\#^* \mu\|^2 - \|\nu\|^2 - 2 \int y^\top w^*(y) d\nu(y) \right], \quad (7)$$

where for any probability measure ρ on \mathbb{R}^d we write $\|\rho\|^2 := \int \|z\|_2^2 d\rho(z)$.

Proof of Theorem 1 Starting from the definition of W_{DF}^{O} and using $\bar{w}^* = -w^*$,

$$W_{\text{DF}}^{\text{O}}(\mu, \nu) = \inf_{\gamma \in \Gamma(\mu, \nu)} \left(- \int y^\top \bar{w}^*(x) d\gamma(x, y) \right) - \int y^\top w^*(y) d\nu(y).$$

Apply Lemma 1 to the measurable map \bar{w}^* (which is still piecewise constant) and to the choice $h(y) := -y$. This gives

$$\inf_{\gamma \in \Gamma(\mu, \nu)} \left(- \int y^\top \bar{w}^*(x) d\gamma(x, y) \right) = \inf_{\bar{\gamma} \in \Gamma((\bar{w}^*)\# \mu, \nu)} \left(- \int y^\top w d\bar{\gamma}(w, y) \right).$$

For any coupling $\bar{\gamma}$ on $\mathbb{R}^d \times \mathbb{R}^d$,

$$\|w - y\|_2^2 = \|w\|_2^2 + \|y\|_2^2 - 2y^\top w \implies -y^\top w = \frac{1}{2} \left(\|w - y\|_2^2 - \|w\|_2^2 - \|y\|_2^2 \right).$$

Since the $\|w\|_2^2$ and $\|y\|_2^2$ terms depend only on the marginals, minimizing $-\int y^\top w d\bar{\gamma}$ over $\Gamma((\bar{w}^*)\# \mu, \nu)$ is equivalent to minimizing $\int \|w - y\|_2^2 d\bar{\gamma}(w, y)$, whose optimum equals $W_2^2((\bar{w}^*)\# \mu, \nu)$. Substituting back and using $\|(\bar{w}^*)\# \mu\|^2 = \|w^* \# \mu\|^2$ yields (7). \square

Theorem 1 shows that the only coupling-dependent term in $W_{\text{DF}}^{\text{O}}(\mu, \nu)$ is the quadratic transport cost between $(\bar{w}^*)\# \mu$ and ν . Importantly, $(\bar{w}^*)\# \mu$ is always discrete, supported on the (finite) set $\{-w_i : w_i \in \mathfrak{S}\}$, even when μ has a continuous density. This reduces computing $W_{\text{DF}}^{\text{O}}(\mu, \nu)$ to a semi-discrete quadratic optimal transport problem when ν is continuous, and to a much smaller discrete OT problem when ν is empirical. After solving the reduced quadratic optimal transport problem, Theorem 2 further establishes a formulation to lift the coupling back to the original space $\Gamma(\mu, \nu)$.

THEOREM 2 (Lifting optimal couplings). *Let $\gamma^* \in \Gamma((\bar{w}^*)\# \mu, \nu)$ be an optimal coupling for the quadratic cost $c(w, y) = \|w - y\|_2^2$ between $(\bar{w}^*)\# \mu$ and ν . Define a measure γ on measurable rectangles by*

$$\gamma(A, B) := \sum_{k=1}^{|\mathfrak{S}|} \gamma^*(\{-w_k\} \times B) \frac{\mu(A \cap D_k)}{\mu(D_k)}, \quad A, B \in \mathcal{B}(\mathbb{R}^d), \quad (8)$$

(with the convention that the k th term is 0 when $\mu(D_k) = 0$). Equivalently,

$$\gamma(D_k \times B) = \gamma^*(\{-w_k\} \times B), \quad k = 1, \dots, |\mathfrak{S}|. \quad (9)$$

Then $\gamma \in \Gamma(\mu, \nu)$ and $W_{\text{SPO}}(\mu, \nu; \gamma) = W_{\text{DF}}^{\text{O}}(\mu, \nu)$.

In Theorem 2, $\gamma^*(\{-w_k\} \times B)$ is the amount of mass that γ^* assigns to pairs (W, Y) with $W = -w_k$ and $Y \in B$. The factor $\mu(A \cap D_k)/\mu(D_k)$ is the conditional probability that $X \in A$ given that $X \in D_k$ under μ (with the convention that the corresponding term is 0 when $\mu(D_k) = 0$). Thus, (8) constructs a coupling $\gamma \in \Gamma(\mu, \nu)$ in the following way: first sampling $(W, Y) \sim \gamma^*$, and whenever $W = -w_k$, sampling X from μ restricted to D_k . This ensures $\bar{w}^*(X) = W$ while preserving the Y -marginal.

REMARK 1. At first glance, minimizing the quadratic cost $c(w, y) = \|w - y\|_2^2$ between $(\bar{w}^*)^* \mu$ and ν may seem counterintuitive. Here, w represents a decision vector (e.g., product recommendations, medication dosages, or path selections), whereas y represents a cost vector (e.g., click-through rates, side effects, or travel times). These two objects may carry different meanings, so subtracting them and minimizing a Euclidean distance can appear unnatural. This reformulation is valid because the coupling-dependent term in $W_{\text{DF}}^{\text{O}}(\mu, \nu)$ depends on x only through $y^\top w^*(x)$. By Lemma 1, optimizing over $\Gamma(\mu, \nu)$ is equivalent (for that term) to optimizing over couplings between the oracle-induced measure and ν , which leads to the quadratic transport objective in Theorem 1.

4.1. Sample complexity via strong duality

In this section, we derive the sample complexity for estimating the DF distance between μ and ν . We consider the standard two-sample setting, where both μ and ν are unknown. We observe independent samples $X_1, \dots, X_{n_\mu} \stackrel{\text{i.i.d.}}{\sim} \mu$ and $Y_1, \dots, Y_{n_\nu} \stackrel{\text{i.i.d.}}{\sim} \nu$, and form the empirical measures $\hat{\mu}_{n_\mu}$ and $\hat{\nu}_{n_\nu}$. The plug-in estimator of the optimistic DF distance is the empirical OT value $W_{\text{DF}}^{\text{O}}(\hat{\mu}_{n_\mu}, \hat{\nu}_{n_\nu})$, computed by solving the empirical linear program in Appendix A. Our goal is to quantify how many samples are required to ensure that the optimistic DF distance computed from the empirical measures is within a tolerance level ϵ of the true optimistic DF distance.

For classical Wasserstein distances W_p , it is well known that estimating $W_p(\mu, \nu)$ from empirical measures typically suffers from the curse of dimensionality: the convergence rate deteriorates as the ambient dimension d grows (e.g., $\mathcal{O}(\sqrt{d}n^{-1/d})$ in Chewi et al. (2025)). In contrast, the optimistic DF distance inherits additional structure from the downstream problem. Because the oracle map $w^*(\cdot)$ takes values in the finite set of extreme points of S , the dependence of W_{DF}^0 on μ is mediated through the finite partition $\{D_i\}$ (equivalently, through the discrete push-forward $w_\#^*\mu$). The strong-duality representation below makes this explicit and leads to sample complexity bounds that depend on $|\mathfrak{S}|$ rather than directly on d .

We first introduce the function space used in the dual. For a probability measure ν on \mathbb{R}^d , let $L^1(\nu)$ denote the set of measurable functions $g : \mathbb{R}^d \rightarrow \mathbb{R}$ such that $\int_{\mathbb{R}^d} |g(y)| \nu(dy) < \infty$.

PROPOSITION 5 (Strong duality for the optimistic DF distance). *Let $\mathfrak{S} = \{w_1, \dots, w_{|\mathfrak{S}|}\}$ be the set of extreme points of S , and let $D_i := \{x \in \mathbb{R}^d : w^*(x) = w_i\}$ denote the oracle regions. Define $z(y) := y^\top w^*(y)$ and, for each i , the reduced cost $c_i(y) := y^\top w_i - z(y)$. Let Φ_{SPO} be the set of all $(f, g) \in \mathbb{R}^{|\mathfrak{S}|} \times L^1(\nu)$ satisfying*

$$f_i + g(y) \leq c_i(y), \quad \forall i \in \{1, \dots, |\mathfrak{S}|\}, \quad \forall y \in \mathbb{R}^d. \quad (10)$$

Then

$$W_{\text{DF}}^0(\mu, \nu) = \sup_{(f, g) \in \Phi_{\text{SPO}}} \left\{ \sum_{i=1}^{|\mathfrak{S}|} f_i \mu(D_i) + \int_{\mathbb{R}^d} g(y) \nu(dy) \right\}. \quad (11)$$

Moreover, for any fixed $f \in \mathbb{R}^{|\mathfrak{S}|}$, the optimal choice of g in (11) is

$$g_f(y) := \min_{1 \leq i \leq |\mathfrak{S}|} (c_i(y) - f_i), \quad (12)$$

and hence (11) can be written equivalently as

$$W_{\text{DF}}^0(\mu, \nu) = \sup_{f \in \mathbb{R}^{|\mathfrak{S}|}} \left\{ \sum_{i=1}^{|\mathfrak{S}|} f_i \mu(D_i) + \int_{\mathbb{R}^d} g_f(y) \nu(dy) \right\}. \quad (13)$$

Proposition 5 shows that the infinite-dimensional coupling optimization can be replaced by a finite-dimensional maximization over $f \in \mathbb{R}^{|\mathfrak{S}|}$, together with an integral of the envelope $g_f(\cdot)$. This structure is what enables dimension-free (in d) dependence on the μ -sample size.

With duality representation, we now state a two-sample concentration result for $W_{\text{DF}}^{\text{O}}(\hat{\mu}_{n_\mu}, \hat{\nu}_{n_\nu})$. Recall that μ and ν are supported on a bounded set $\mathcal{Y} \subset \mathbb{R}^d$, and S is compact with diameter D_W . Under these assumptions, ℓ_{SPO} is uniformly bounded by $B := \|\mathcal{Y}\|D_W < \infty$.

THEOREM 3 (Two-sample concentration for W_{DF}^{O}). *For any $\delta \in (0, 1)$, with probability at least $1 - \delta$,*

$$\left| W_{\text{DF}}^{\text{O}}(\hat{\mu}_{n_\mu}, \hat{\nu}_{n_\nu}) - W_{\text{DF}}^{\text{O}}(\mu, \nu) \right| \leq B \sqrt{\frac{|\mathfrak{S}|}{n_\mu}} + C B \sqrt{\frac{|\mathfrak{S}|}{n_\nu}} + 2B \sqrt{\frac{\log(4/\delta)}{2n_\mu}} + 2B \sqrt{\frac{\log(4/\delta)}{2n_\nu}}, \quad (14)$$

where $C > 0$ is a universal constant.

The bound in Theorem 3 immediately implies an ϵ -accuracy sample complexity, which also applies to the Robust DF case. Ignoring logarithmic factors in δ and constants, the dominant terms scale as $B\sqrt{|\mathfrak{S}|/n_\mu}$ and $CB\sqrt{|\mathfrak{S}|/n_\nu}$. Compared with the typical convergence rate for estimating the classical W_p distance in high dimensions, which scales on the order of $O(\sqrt{d}n^{-1/d})$, the resulting rate for the DF distance is substantially faster and, notably, independent of the ambient dimension d . To guarantee $|W_{\text{DF}}^{\text{O}}(\hat{\mu}_{n_\mu}, \hat{\nu}_{n_\nu}) - W_{\text{DF}}^{\text{O}}(\mu, \nu)| \leq \epsilon$ with high probability, it suffices to take $n_\mu = \tilde{O}\left(\frac{B^2|\mathfrak{S}|}{\epsilon^2}\right)$, and $n_\nu = \tilde{O}\left(\frac{B^2|\mathfrak{S}|}{\epsilon^2}\right)$, where $\tilde{O}(\cdot)$ suppresses logarithmic dependence on $1/\delta$.

Proof of Theorem 3 We proceed in three steps.

Step 1: Dual representations for population and empirical objectives. By Proposition 5, we may write

$$W_{\text{DF}}^{\text{O}}(\mu, \nu) = \sup_{f \in \mathbb{R}^{|\mathfrak{S}|}} \left\{ \sum_{i=1}^{|\mathfrak{S}|} f_i \mu(D_i) + \mathbb{E}[g_f(Y)] \right\}, \quad (15)$$

where $Y \sim \nu$ and g_f is given by (12). Likewise,

$$W_{\text{DF}}^{\text{O}}(\hat{\mu}_{n_\mu}, \hat{\nu}_{n_\nu}) = \sup_{f \in \mathbb{R}^{|\mathfrak{S}|}} \left\{ \sum_{i=1}^{|\mathfrak{S}|} f_i \hat{\mu}_{n_\mu}(D_i) + \frac{1}{n_\nu} \sum_{j=1}^{n_\nu} g_f(Y_j) \right\}. \quad (16)$$

Since the SPO loss is uniformly bounded by B , we have $0 \leq c_i(y) \leq B$ for all i and $y \in \mathcal{Y}$, hence $0 \leq g_f(y) \leq B$ whenever $\max_i f_i = 0$. Moreover, the dual objective is invariant under the shift $f \mapsto f + t\mathbf{1}$ (because $\sum_i \mu(D_i) = 1$ and $\sum_i \hat{\mu}_{n_\mu}(D_i) = 1$), so we may restrict the supremum in (15)–(16) to the normalized set

$$\mathcal{F} := \left\{ f \in \mathbb{R}^{|\mathfrak{S}|} : \max_{1 \leq i \leq |\mathfrak{S}|} f_i = 0, \min_{1 \leq i \leq |\mathfrak{S}|} f_i \geq -B \right\},$$

without changing either value. In particular, for $f \in \mathcal{F}$ we have $|f_i| \leq B$ and $0 \leq g_f(y) \leq B$.

Step 2: Decomposing the estimation error. For each $f \in \mathcal{F}$, define

$$A(f) := \sum_{i=1}^{|\mathfrak{S}|} f_i \hat{\mu}_{n_\mu}(D_i) + \frac{1}{n_\nu} \sum_{j=1}^{n_\nu} g_f(Y_j), \quad B(f) := \sum_{i=1}^{|\mathfrak{S}|} f_i \mu(D_i) + \mathbb{E}[g_f(Y)].$$

By the dual representations (16)–(15), we have

$$W_{\text{DF}}^{\text{O}}(\hat{\mu}_{n_\mu}, \hat{\nu}_{n_\nu}) = \sup_{f \in \mathcal{F}} A(f), \quad W_{\text{DF}}^{\text{O}}(\mu, \nu) = \sup_{f \in \mathcal{F}} B(f).$$

We first upper bound the difference $W_{\text{DF}}^{\text{O}}(\hat{\mu}_{n_\mu}, \hat{\nu}_{n_\nu}) - W_{\text{DF}}^{\text{O}}(\mu, \nu)$. Write

$$W_{\text{DF}}^{\text{O}}(\hat{\mu}_{n_\mu}, \hat{\nu}_{n_\nu}) - W_{\text{DF}}^{\text{O}}(\mu, \nu) = \sup_{f \in \mathcal{F}} A(f) - \sup_{f \in \mathcal{F}} B(f).$$

Using the inequality $\sup_f A_f - \sup_f B_f \leq \sup_f (A_f - B_f)$, we obtain

$$\begin{aligned} W_{\text{DF}}^{\text{O}}(\hat{\mu}_{n_\mu}, \hat{\nu}_{n_\nu}) - W_{\text{DF}}^{\text{O}}(\mu, \nu) &\leq \sup_{f \in \mathcal{F}} (A(f) - B(f)) \\ &= \sup_{f \in \mathcal{F}} \left\{ \sum_{i=1}^{|\mathfrak{S}|} f_i (\hat{\mu}_{n_\mu}(D_i) - \mu(D_i)) + \left(\frac{1}{n_\nu} \sum_{j=1}^{n_\nu} g_f(Y_j) - \mathbb{E}[g_f(Y)] \right) \right\} \\ &\leq \sup_{f \in \mathcal{F}} \left| \sum_{i=1}^{|\mathfrak{S}|} f_i (\hat{\mu}_{n_\mu}(D_i) - \mu(D_i)) \right| + \sup_{f \in \mathcal{F}} \left| \frac{1}{n_\nu} \sum_{j=1}^{n_\nu} g_f(Y_j) - \mathbb{E}[g_f(Y)] \right|. \end{aligned}$$

We next upper bound the difference in the reverse direction. Similarly,

$$W_{\text{DF}}^{\text{O}}(\mu, \nu) - W_{\text{DF}}^{\text{O}}(\hat{\mu}_{n_\mu}, \hat{\nu}_{n_\nu}) = \sup_{f \in \mathcal{F}} B(f) - \sup_{f \in \mathcal{F}} A(f) \leq \sup_{f \in \mathcal{F}} (B(f) - A(f)).$$

Repeating the same expansion and triangle inequality yields the same upper bound,

$$W_{\text{DF}}^{\text{O}}(\mu, \nu) - W_{\text{DF}}^{\text{O}}(\hat{\mu}_{n_\mu}, \hat{\nu}_{n_\nu}) \leq \sup_{f \in \mathcal{F}} \left| \sum_{i=1}^{|\mathfrak{S}|} f_i (\hat{\mu}_{n_\mu}(D_i) - \mu(D_i)) \right| + \sup_{f \in \mathcal{F}} \left| \frac{1}{n_\nu} \sum_{j=1}^{n_\nu} g_f(Y_j) - \mathbb{E}[g_f(Y)] \right|.$$

Combining the two one-sided bounds, we conclude that

$$\left| W_{\text{DF}}^{\text{O}}(\hat{\mu}_{n_\mu}, \hat{\nu}_{n_\nu}) - W_{\text{DF}}^{\text{O}}(\mu, \nu) \right| \leq \Delta_\mu + \Delta_\nu, \quad (17)$$

where

$$\Delta_\mu := \sup_{f \in \mathcal{F}} \left| \sum_{i=1}^{|\mathfrak{S}|} f_i (\hat{\mu}_{n_\mu}(D_i) - \mu(D_i)) \right|, \quad \Delta_\nu := \sup_{f \in \mathcal{F}} \left| \frac{1}{n_\nu} \sum_{j=1}^{n_\nu} g_f(Y_j) - \mathbb{E}[g_f(Y)] \right|.$$

We bound Δ_μ and Δ_ν separately.

Step 3: Concentration for Δ_μ and Δ_ν . For Δ_μ , since $|f_i| \leq B$ for $f \in \mathcal{F}$,

$$\Delta_\mu \leq B \sum_{i=1}^{|\mathfrak{S}|} |\hat{\mu}_{n_\mu}(D_i) - \mu(D_i)|.$$

Let $p_i := \mu(D_i)$ and $\hat{p}_i := \hat{\mu}_{n_\mu}(D_i)$. Then

$$\mathbb{E}[\Delta_\mu] \leq B \mathbb{E} \left[\|\hat{p} - p\|_1 \right] \leq B \sqrt{|\mathfrak{S}|} \left(\mathbb{E} \|\hat{p} - p\|_2^2 \right)^{1/2}.$$

Moreover, we can bound the second moment of $\hat{p} - p$ as follows. First,

$$\mathbb{E} \|\hat{p} - p\|_2^2 = \mathbb{E} \left[\sum_{i=1}^{|\mathfrak{S}|} (\hat{p}_i - p_i)^2 \right] = \sum_{i=1}^{|\mathfrak{S}|} \mathbb{E} [(\hat{p}_i - p_i)^2] = \sum_{i=1}^{|\mathfrak{S}|} \text{Var}(\hat{p}_i),$$

where we use $\mathbb{E}[\hat{p}_i] = p_i$ for each i . Next, since $\hat{p}_i = \frac{1}{n_\mu} \sum_{t=1}^{n_\mu} \mathbf{1}\{X_t \in D_i\}$, we have

$$\text{Var}(\hat{p}_i) = \text{Var} \left(\frac{1}{n_\mu} \sum_{t=1}^{n_\mu} \mathbf{1}\{X_t \in D_i\} \right) = \frac{1}{n_\mu} \text{Var}(\mathbf{1}\{X_1 \in D_i\}) = \frac{1}{n_\mu} p_i (1 - p_i).$$

Therefore,

$$\mathbb{E} \|\hat{p} - p\|_2^2 = \sum_{i=1}^{|\mathfrak{S}|} \text{Var}(\hat{p}_i) = \frac{1}{n_\mu} \sum_{i=1}^{|\mathfrak{S}|} p_i (1 - p_i) \leq \frac{1}{n_\mu} \sum_{i=1}^{|\mathfrak{S}|} p_i = \frac{1}{n_\mu},$$

and therefore

$$\mathbb{E}[\Delta_\mu] \leq B \sqrt{\frac{|\mathfrak{S}|}{n_\mu}}. \quad (18)$$

In addition, changing one sample X_t alters each \hat{p}_i by at most $1/n_\mu$, hence changes Δ_μ by at most $2B/n_\mu$. McDiarmid's inequality yields that with probability at least $1 - \delta/2$,

$$\Delta_\mu \leq \mathbb{E}[\Delta_\mu] + 2B \sqrt{\frac{\log(4/\delta)}{2n_\mu}}. \quad (19)$$

For Δ_ν , note that $0 \leq g_f(y) \leq B$ for all $f \in \mathcal{F}$ and $y \in \mathcal{Y}$. A standard symmetrization and Rademacher complexity bound for the class $\{g_f : f \in \mathcal{F}\}$ gives

$$\mathbb{E}[\Delta_\nu] \leq C B \sqrt{\frac{|\mathfrak{S}|}{n_\nu}} \quad (20)$$

for a universal constant $C > 0$. Moreover, changing one sample Y_t changes the empirical average $\frac{1}{n_\nu} \sum_{j=1}^{n_\nu} g_f(Y_j)$ by at most B/n_ν uniformly over f , hence changes Δ_ν by at most $2B/n_\nu$. McDiarmid's inequality yields that with probability at least $1 - \delta/2$,

$$\Delta_\nu \leq \mathbb{E}[\Delta_\nu] + 2B \sqrt{\frac{\log(4/\delta)}{2n_\nu}}. \quad (21)$$

Finally, combining (17) with (18)–(21) and applying a union bound over the events in (19) and (21) yields (14). \square

5. Applications: Decision-focused Interpolation

In this section, we illustrate an application of the DF divergence to distributional interpolation. Intuitively, in a decision-focused setting, given two measures μ and ν , a meaningful “average” should not be the naive mixture $(\mu + \nu)/2$. Instead, it should account for how probability mass under μ is matched to probability mass under ν , and this matching depends on the downstream oracle map $w^*(\cdot)$ through the decision loss.

McCann's interpolation (McCann (1997)) provides a canonical way to construct a path of intermediate measures between two endpoints via an optimal coupling. The basic mechanism is as

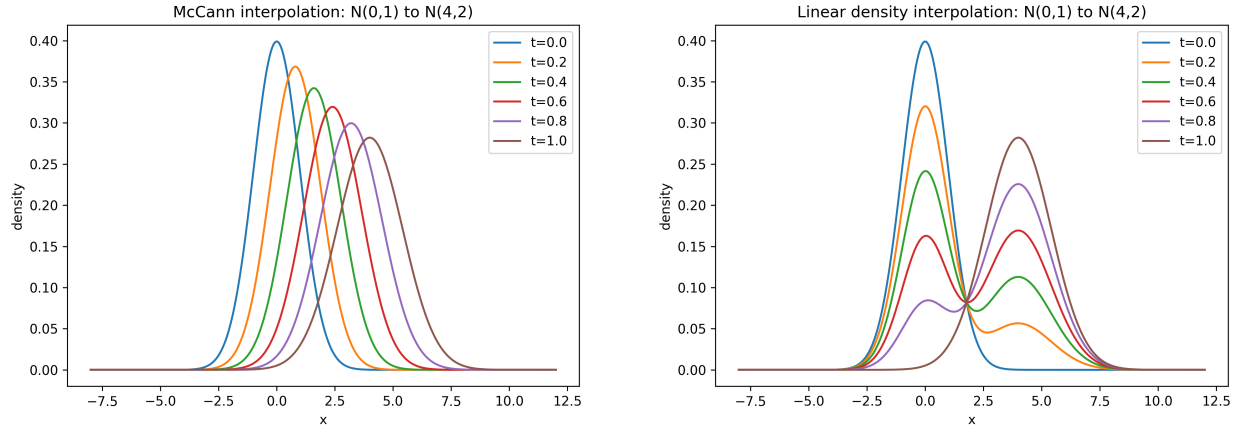
follows: one first selects an optimal coupling between the endpoint measures and then pushes that coupling forward through the linear map $\pi_t(x, y) = (1 - t)x + ty$ for $t \in [0, 1]$. In the classical quadratic OT setting, this recovers the McCann (displacement) interpolation and produces a constant-speed geodesic in $(\mathcal{P}_2(\mathbb{R}^d), W_2)$. In our decision-focused setting, the cost ℓ_{SPO} is generally non-quadratic (and may be discontinuous through $w^*(\cdot)$), so a direct W_2 -geodesic interpretation does not hold in general. Nevertheless, optimal couplings for W_{DF}^{O} and W_{DF}^{R} still induce canonical families of intermediate measures through the same push-forward construction. Section 5.1 provides the basic formulation of McCann interpolation.

5.1. McCann interpolation from an optimal coupling

Let $\mu_0, \mu_1 \in \mathcal{P}_2(\mathbb{R}^d)$, and let $\gamma \in \Gamma(\mu_0, \mu_1)$ be an optimal coupling for the quadratic cost $c(x, y) = \|x - y\|_2^2$. For $t \in [0, 1]$, define $\pi_t(x, y) = (1 - t)x + ty$ and set $\mu_t := (\pi_t)_\# \gamma$. Equivalently, for any Borel set $A \subseteq \mathbb{R}^d$, $\mu_t(A) = \gamma(\{(x, y) : (1 - t)x + ty \in A\})$. This definition does not require the existence of an optimal transport map; in general, the coupling γ allows mass from μ_0 to split across multiple destinations in μ_1 . To motivate McCann interpolation, we consider the following example.

EXAMPLE 1 (MIXTURE INTERPOLATION VS. McCANN INTERPOLATION). Let $\mu_0 = \mathcal{N}(0, 1)$ and $\mu_1 = \mathcal{N}(4, 2)$ on \mathbb{R} . A naive interpolation linearly averages the densities, $p_t = (1 - t)p_{\mu_0} + tp_{\mu_1}$, which yields a two-component Gaussian mixture and can be bimodal for intermediate t . In contrast, the McCann interpolation in $(\mathcal{P}_2(\mathbb{R}), W_2)$ transports mass along an optimal coupling and remains Gaussian for all $t \in [0, 1]$, with $\mu_t = \mathcal{N}(4t, ((1 - t) + t\sqrt{2})^2)$.

Figure 4 compares the McCann interpolation with the naive density mixture between μ_0 and μ_1 as t varies from 0 to 1. The McCann interpolant shown in the left panel preserves the Gaussian shape throughout the transition from μ_0 to μ_1 , whereas the naive density mixture in the right panel becomes bimodal at intermediate values of t . In practice, when the distributional shape is preserved



(a) McCann (displacement) interpolation (b) Linear density averaging $p_t = (1 - t)p_{N(0,1)} + t p_{N(4,2)}$.

Figure 4 Comparison of McCann interpolation and linear density averaging for Gaussian measures. Left: McCann interpolation captures a smooth displacement from μ_0 to μ_1 . Right: linear density averaging can be bimodal for intermediate t and does not reflect a plausible transport of mass.

along the dynamics, McCann interpolation provides a more realistic estimate of the intermediate path by considering an optimal coupling.

5.2. Decision-focused interpolations

We now define decision-focused interpolants by pushing forward optimal couplings of the DF objectives through the same linear map $\pi_t(x, y) = (1 - t)x + ty$. Unlike the quadratic setting, these interpolants are not geodesics for a Riemannian-type metric in the data space; rather, they provide a coupling-driven path from μ_0 to μ_1 that is tailored to decision loss.

DEFINITION 5 (DECISION-FOCUSED INTERPOLANT INDUCED BY A COUPLING). Let $\mu_0, \mu_1 \in \mathcal{P}_2(\mathbb{R}^d)$, let $\gamma \in \Gamma(\mu_0, \mu_1)$ be any coupling, and for $t \in [0, 1]$ define $\pi_t(x, y) = (1 - t)x + ty$. The *decision-focused interpolant* induced by γ at time t is

$$\mu_t^\gamma := (\pi_t)_\# \gamma, \quad t \in [0, 1].$$

In Definition 5, varying t from 0 to 1 yields a path of intermediate distributions that transforms μ_0 into μ_1 under the coupling γ . In a decision-focused setting, the coupling γ is chosen to reflect

the desired decision-focused objective. For instance, one may take γ to be an optimizer of the Optimistic DF distance, an optimizer of Robust DF distance, or an optimizer of the entropy-regularized formulations (E-DFO)–(E-DFR). Each choice yields a different interpolation path $\{\mu_t^\gamma\}_{t \in [0,1]}$, reflecting different coupling structures between μ_0 and μ_1 .

REMARK 2. The interpolant in Definition 5 is constructed by pushing forward a coupling $\gamma \in \Gamma(\mu_0, \mu_1)$. Recall that Section 4 provides a W_2 reduction of the optimistic DF distance in terms of couplings in the reduced space $\Gamma(w_\#^* \mu_0, \mu_1)$. Accordingly, one may alternatively construct an interpolation in the reduced space $\Gamma(w_\#^* \mu_0, \mu_1)$ and then lift it back to a coupling in $\Gamma(\mu_0, \mu_1)$. This procedure generally produces a different interpolation path from that in Definition 5. We compare the two approaches in Appendix C. In practice, we recommend using Definition 5, as the resulting path directly describes the evolution from μ_0 to μ_1 in the original data space and is easier to interpret than a path constructed between $w_\#^* \mu_0$ and μ_1 in the reduced space.

THEOREM 4 (A one-sided bound along the optimistic DF interpolant). *Let μ, ν be probability measures on \mathbb{R}^d with finite second moments. Let $\gamma^* \in \Gamma(\mu, \nu)$ be an optimizer for $W_{\text{DF}}^O(\mu, \nu)$, and for $t \in [0, 1]$ define $\pi_t(u, v) = (1 - t)u + tv$ and $\nu_t := (\pi_t)_\# \gamma^*$. Then, for all $t \in [0, 1]$, we have*

$$W_{\text{DF}}^O(\mu, \nu_t) \leq t W_{\text{DF}}^O(\mu, \nu).$$

Theorem 4 provides a simple “constant-speed” upper bound along the optimistic DF interpolant: as t increases from 0 to 1, the decision-focused distance from μ to the intermediate marginal ν_t grows at most linearly, i.e., $W_{\text{DF}}^O(\mu, \nu_t) \leq t W_{\text{DF}}^O(\mu, \nu)$. This mirrors the exact constant-speed property of the McCann geodesic for W_2 , but only in a one-sided form (for the W_2 McCann interpolation, the speed is exactly constant; see Appendix C). As shown in the proof, this inequality $W_{\text{DF}}^O(\mu, \nu_t) \leq t W_{\text{DF}}^O(\mu, \nu)$ stems from the concavity of the value function $z(x) = \min_{w \in S} w^\top x$. Practically, the result guarantees that the optimistic DF interpolant yields a family of distributions whose decision-focused discrepancy from μ is controlled uniformly in t , which is useful when generating intermediate

distributions (e.g., for data augmentation or gradual shift modeling) while maintaining bounded decision degradation. As a special case, if γ is an optimal coupling for $W_{\text{DF}}^0(\mu_0, \mu_1)$ and $t = \frac{1}{2}$, we refer to the resulting measure $\mu_{1/2}^\gamma$ as the *decision-focused average* of μ_0 and μ_1 .

6. Numerical Study

This section evaluates the proposed decision-focused divergences and the coupling-induced interpolations on both synthetic and real data. We first present an illustrative example based on the single-period newsvendor problem, which compares the values of different distance metrics for different pairs of distributions. We then study a real longitudinal healthcare dataset to quantify distributional change over time, construct intermediate-time distributions via coupling-induced interpolation, and evaluate downstream decision quality through the SPO loss.

6.1. Toy example for newsvendor problem

We use the single-period newsvendor problem as a simple downstream decision task to illustrate the behavior of the decision-focused divergences relative to standard distributional distances. Although the classical newsvendor is often written as a scalar minimization over an order quantity, it can be embedded into our linear optimization framework by allowing randomized ordering decisions over a finite set of feasible order quantities.

Specifically, demand takes values in a finite set $\{d_i : i \in I\}$, where $I = \{1, \dots, m\}$, with $\mathbb{P}(D = d_i) = p_i$ and $\sum_{i \in I} p_i = 1$. The decision-maker chooses an order quantity from a discrete set $\{q_j : j \in J\}$, where $J = \{1, \dots, n\}$. If demand realizes as d_i and the order quantity is q_j , the incurred cost is C_{ij} , where the matrix $(C_{ij})_{i \in I, j \in J}$ is assumed known (and can encode purchasing, holding, shortage, or other operational penalties). The decision vector $x = (x_j)_{j \in J}$ denote the probability of choosing each order quantity q_j . Thus, $x_j \in [0, 1]$ and x lies in the simplex. The expected cost is

linear in x , and the newsvendor problem can be written as the linear program

$$\begin{aligned} \min_x \quad & \sum_{i \in I} \sum_{j \in J} p_i C_{ij} x_j \\ \text{s.t.} \quad & \sum_{j \in J} x_j = 1, \\ & x_j \geq 0, \quad \forall j \in J. \end{aligned} \quad (22)$$

The extreme points of (22) correspond to deterministic ordering decisions.

We now specialize to the standard underage–overage structure. Let $b > 0$ and $h > 0$ denote the unit underage (shortage) and overage (holding) costs, respectively, and define the critical fractile $\alpha := \frac{b}{b+h}$. In the example below, we set $\alpha = 0.6$ by choosing $b = 3$ and $h = 2$. For customer type $k \in \{1, 2, 3\}$ with demand distribution μ_k and CDF $F^{(k)}$, the optimal order quantity refers to the 60% quantile value.

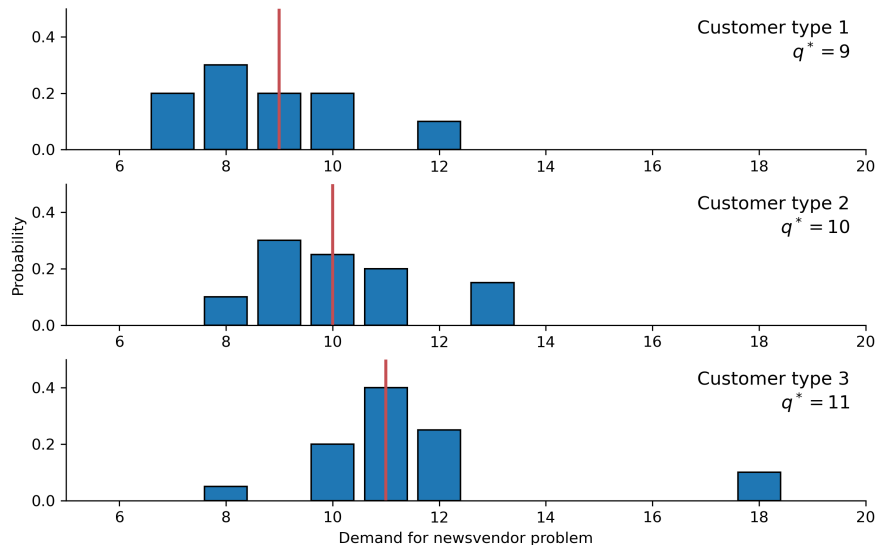


Figure 5 Three customer types have distinct discrete demand distributions and, under $\alpha = 0.6$, induce distinct optimal order quantities $q^{*(1)} = 9$, $q^{*(2)} = 10$, and $q^{*(3)} = 11$ (vertical red lines).

Figure 5 shows three discrete demand distributions μ_1, μ_2, μ_3 with different shapes and different α -quantiles. In particular, for $\alpha = 0.6$ we obtain $q^{*(1)} = 9$, $q^{*(2)} = 10$, and $q^{*(3)} = 11$. Thus, the customer type affects the downstream optimal decision.

To connect with our decision-focused OT formulation, we treat the population as heterogeneous: a random arriving customer belongs to type $k \in \{1, 2, 3\}$ with probability λ_k .

We further consider population mixtures of the three customer types. Let $\lambda = (\lambda_1, \lambda_2, \lambda_3) \in \Delta_3$ denote mixture weights and define $\mu_\lambda := \sum_{k=1}^3 \lambda_k \delta_{c^{(k)}}$. We take the uniform mixture $\lambda_0 = (1/3, 1/3, 1/3)$ as a baseline population. Table 1 reports several distance measures between μ_λ and μ_{λ_0} for different mixture vectors λ , including decision-focused distances $W_{\text{DF}}^{\text{O}}(\mu_\lambda, \mu_{\lambda_0})$ and $W_{\text{DF}}^{\text{R}}(\mu_\lambda, \mu_{\lambda_0})$. In Table 1, the column $R(\mu_\lambda, \mu_{\lambda_0})$ reports the decision-focused risk under the independent coupling $\mu_\lambda \otimes \mu_{\lambda_0}$ (i.e., expected SPO loss when type draws are independent). TV and KL are computed directly on the weights. The Wasserstein distances W_1 and W_2 are computed on the three-point type space $\{1, 2, 3\}$ with ground cost $|i - j|$ (for W_1) and $|i - j|^2$ (for W_2).

$\lambda = (\lambda_1, \lambda_2, \lambda_3)$	W_{DF}^{O}	$R(\mu_\lambda, \mu_{\lambda_0})$	W_{DF}^{R}	TV	KL($\lambda \parallel \lambda_0$)	W_1	W_2
$(\frac{1}{4}, \frac{1}{4}, \frac{1}{2})$	0.0833	1.0208	1.9792	0.1667	0.0589	0.2500	0.5000
$(\frac{1}{5}, \frac{1}{5}, \frac{3}{5})$	0.1333	0.9667	1.8667	0.2667	0.1483	0.4000	0.6325
$(\frac{1}{6}, \frac{1}{6}, \frac{2}{3})$	0.1667	0.9306	1.7917	0.3333	0.2310	0.5000	0.7071
$(\frac{1}{10}, \frac{1}{10}, \frac{8}{10})$	0.4000	0.8583	1.3750	0.4667	0.4596	0.7000	0.9832

Table 1 Various Distances between mixture-weight vectors λ and the baseline $\lambda_0 = (1/3, 1/3, 1/3)$.

In Table 1, as the row index increases, the distribution λ becomes increasingly imbalanced. In this regime, the optimistic DF distance, d_{TV} , KL divergence, and the Wasserstein distances W_1 and W_2 all increase, reflecting a larger geometric discrepancy induced by the growing imbalance. On the other hand, W_{DF}^{R} captures the worst-case alignment of customer types between the two populations and decreases as the imbalance becomes more pronounced. As expected, we observe $W_{\text{DF}}^{\text{O}}(\mu_\lambda, \mu_{\lambda_0}) \leq R(\mu_\lambda, \mu_{\lambda_0}) \leq W_{\text{DF}}^{\text{R}}(\mu_\lambda, \mu_{\lambda_0})$, and the gap between W_{DF}^{O} and W_{DF}^{R} can be substantial.

6.2. Real-data analysis on Parkinson's disease

This subsection evaluates the proposed decision-focused divergences and interpolants on the real-world *Parkinson's Telemonitoring* dataset, which contains repeated measurements per patient. The numerical evaluation focuses on three perspectives: (i) constructing intermediate-time distributions via decision-focused interpolations (Section 5); (ii) evaluating the impact of the entropy regularization term in optimal transport (Proposition 4); and (iii) examining the estimation error rate as a function of sample size (Theorem 3).

6.2.1. Dataset and problem setup. We use the Parkinson's Telemonitoring dataset from the UCI repository, which contains 5,875 total observations from 42 Parkinson's disease patients. Each observation includes a measurement time (days from study start), two clinical severity measures, `motor_UPDRS` and `total_UPDRS`, and multiple voice-related features. The data are longitudinal, as the same patient is measured repeatedly over time. This structure enables both population-level distribution comparisons and patient-tracked evaluations. We focus on patients' disease progression over the following three time windows: $[t - 5, t + 5]$ for $t \in \{50, 100, 150\}$.

For the decision-making problem, the decision variable is a weekly care plan

$$w = (h_{\text{exercise}}, h_{\text{nursing}}, h_{\text{rest}}, h_{\text{speech}}) \in \mathbb{R}^4,$$

where each coordinate represents the hours per week allocated to a care modality: physical exercise or physiotherapy, nursing or care coordination, sleep or rest optimization, and speech therapy. The objective is to minimize $y^\top w$, where

$$y = (y_{\text{ex}}, y_{\text{nurse}}, y_{\text{rest}}, y_{\text{speech}}) \in \mathbb{R}^4$$

is constructed from two severity measures and two additional covariates, (`motor_UPDRS`, `total_UPDRS`, `age`, `PPE`). The detailed data processing procedure is provided in

Appendix E. The feasible region consists of five candidate therapy plans, which are also detailed in Appendix E. Before analyzing couplings across different days, Figure 6 illustrates the joint density of two selected variables across the 42 patients.

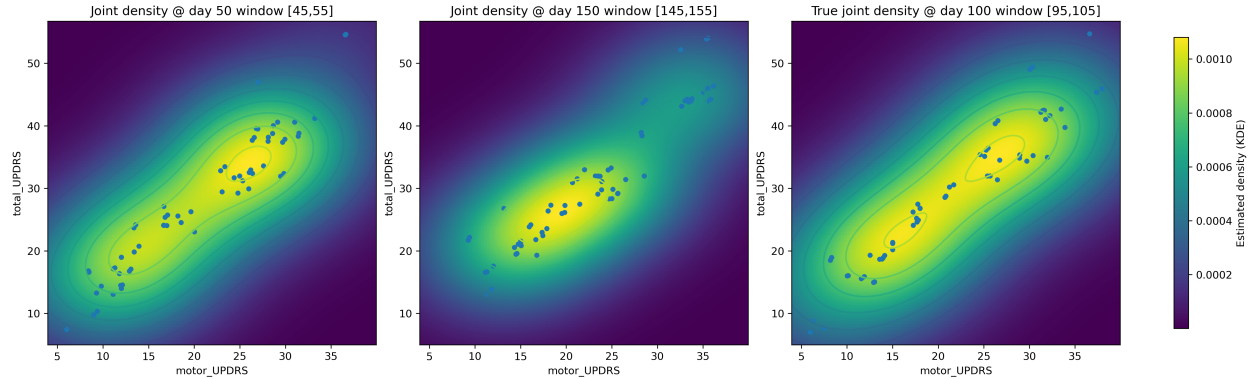


Figure 6 Empirical distribution of patients during three different periods.

When we evaluate the average decision loss (SPO loss) between Day 50 and Day 150, the traditional method directly plugs in the marginal distributions at the two time points, without considering the coupling, yielding an average regret of $R(\hat{\mu}_{50}, \hat{\nu}_{150}) \approx 0.4566$. However, in practice, if we track each patient and average the SPO loss across patients between Day 50 and Day 150, the regret is only 0.0359, with a median of 0. This order-of-magnitude gap indicates that independent evaluations that ignore temporal alignment can substantially overestimate risk in practice, which motivates explicitly modeling couplings across time.

6.2.2. Decision-focused interpolations. We first implement McCann interpolations for optimistic, robust, and independent decision-focused couplings without regularization. In particular, we use the distributions around Day 50 and Day 150 to interpolate the distribution around Day 100. Numerical details are provided in Appendix E. The predicted densities, together with the true density, are shown in Figure 7.

Figure 7 shows that the optimistic decision-focused interpolation is closest to the true distribution. This result aligns with the intuition that each patient's disease progression depends on their current

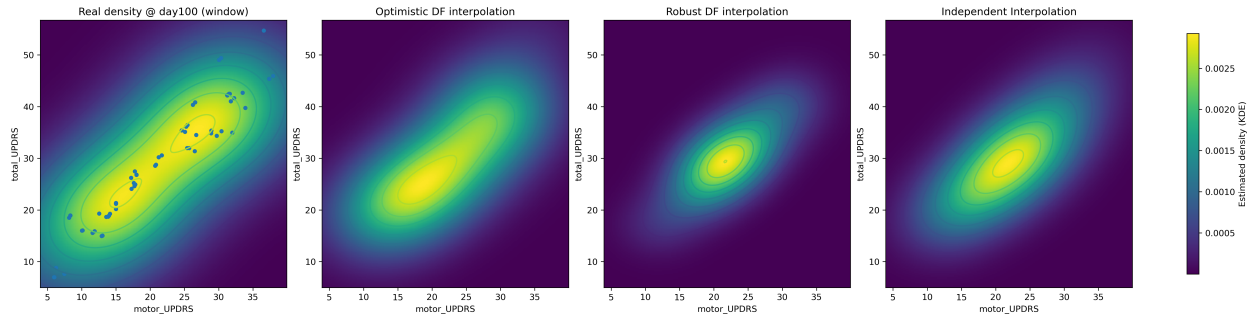


Figure 7 Predicted distributions obtained via decision-focused interpolations.

status, whereas interpolations based on the entire population may induce larger deviations at the individual level.

6.2.3. Entropy regularization. Recall that Proposition 4 shows that introducing entropy regularization yields interpolations that lie between the extreme optimistic and robust cases. We therefore add an entropy regularization term and vary the value of ϵ . The average SPO loss, evaluated by tracking each patient using the observed data around Day 100, is reported in Figure 8.

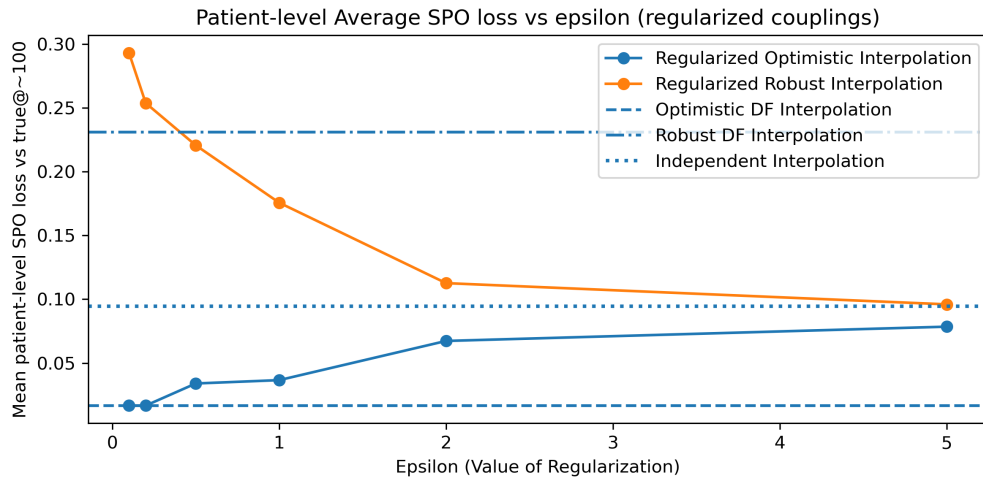


Figure 8 Impact of entropy regularization on decision-focused interpolation. SPO loss is evaluated by tracking each patient.

Figure 8 shows that as the regularization parameter ϵ increases, the performance of decision-focused interpolations approaches that of the independent interpolation. Since the evaluation is

based on real patient trajectories, the optimistic and robust cases do not necessarily provide uniform upper or lower bounds for all values of ϵ , especially when ϵ is small.

6.2.4. Estimation error rates. Theorem 3 establishes an estimation error bound of order $\tilde{O}(1/n)$ for coupling estimation. To illustrate this result, we visualize the estimation error as a function of sample size. The estimation error curves are shown in Figure 9.

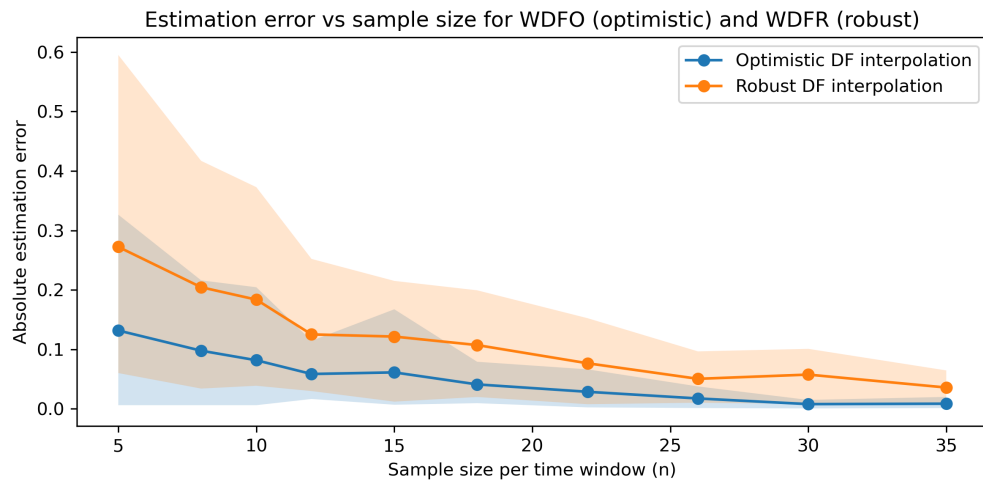


Figure 9 Estimation error for McCann interpolations.

Figure 9 demonstrates that the estimation error converges effectively to zero as the sample size increases. The results also indicate that the robust decision-focused interpolation exhibits a larger estimation error than the optimistic one. For additional results and details of the numerical study, please refer to Appendix E.

7. Conclusion

In this paper, we propose a new metric to quantify distances between distributions in stochastic optimization problems. The proposed decision-focused distance is closely related to classical metrics such as total variation, KL divergence, and Wasserstein distance. We develop efficient algorithms for computing this distance and derive dimension-independent estimation error bounds. Real-world numerical experiments further demonstrate the value of the proposed decision-focused divergence.

This metric provides a foundation for future work on decision-focused clustering, anomaly detection, regression, uncertainty set construction, and related problems in stochastic optimization.

Acknowledgments

We thank Dr. Soumik Pal for his insightful feedback on this paper during his visit to Chapel Hill. Suhan Liu acknowledges financial support from the National Science Foundation [Grant DMS-2450005].

References

Bennouna A, Van Parys B (2022) Holistic robust data-driven decisions. *arXiv preprint arXiv:2207.09560* .

Bertsimas D, Kallus N (2020) From predictive to prescriptive analytics. *Management Science* 66(3):1025–1044.

Blanchet J, Murthy K (2019) Quantifying distributional model risk via optimal transport. *Mathematics of Operations Research* 44(2):565–600.

Blanchet J, Murthy K, Zhang F (2022) Optimal transport-based distributionally robust optimization: Structural properties and iterative schemes. *Mathematics of Operations Research* 47(2):1500–1529.

Chewi S, Niles-Weed J, Rigollet P (2025) *Statistical Optimal Transport*, volume 2364 of *Lecture Notes in Mathematics* (Springer Cham), ISBN 978-3-031-85159-9, URL <http://dx.doi.org/10.1007/978-3-031-85160-5>.

Cristian R, Harsha P, Perakis G, Quanz B (2025) Efficient end-to-end learning for decision-making: A meta-optimization approach. *arXiv preprint arXiv:2505.11360* .

El Balghiti O, Elmachtoub AN, Grigas P, Tewari A (2022) Generalization bounds in the predict-then-optimize framework. *Mathematics of Operations Research* .

Elmachtoub AN, Grigas P (2022) Smart “predict, then optimize”. *Management Science* 68(1):9–26.

Elmachtoub AN, Lam H, Lan H, Zhang H (2025) Dissecting the impact of model misspecification in data-driven optimization. *arXiv preprint arXiv:2503.00626* .

Elmachtoub AN, Lam H, Zhang H, Zhao Y (2023) Estimate-then-optimize versus integrated-estimation-optimization: A stochastic dominance perspective. *arXiv preprint arXiv:2304.06833* 107.

Er C, Liu M (2025) Decision-focused bias correction for fluid approximation. *arXiv preprint arXiv:2512.15726* .

Gao R (2023) Finite-sample guarantees for wasserstein distributionally robust optimization: Breaking the curse of dimensionality. *Operations Research* 71(6):2291–2306.

Gao R, Chen X, Kleywegt AJ (2024) Wasserstein distributionally robust optimization and variation regularization. *Operations Research* 72(3):1177–1191.

Ho-Nguyen N, Kilinç-Karzan F, Küçükyavuz S, Lee D (2023) Strong formulations for distributionally robust chance-constrained programs with left-hand side uncertainty under wasserstein ambiguity. *INFORMS Journal on Optimization* 5(2):211–232.

Homem-de Mello T, Valencia J, Lagos F, Lagos G (2024) Forecasting outside the box: Application-driven optimal pointwise forecasts for stochastic optimization. *arXiv preprint arXiv:2411.03520*.

Hu Y, Kallus N, Mao X (2022) Fast rates for contextual linear optimization. *Management Science* 68(6):4236–4245.

Huang M, Gupta V (2024) Decision-focused learning with directional gradients. *Advances in Neural Information Processing Systems* 37:79194–79220.

Kuhn D, Esfahani PM, Nguyen VA, Shafieezadeh-Abadeh S (2019) Wasserstein distributionally robust optimization: Theory and applications in machine learning. *Operations research & management science in the age of analytics*, 130–166 (Informs).

Liu M, Grigas P, Liu H, Shen ZJM (2023) Active learning in the predict-then-optimize framework: A margin-based approach. *arXiv preprint arXiv:2305.06584*.

Mandi J, Kotary J, Berden S, Mulamba M, Bucarey V, Guns T, Fioretto F (2024) Decision-focused learning: Foundations, state of the art, benchmark and future opportunities. *Journal of Artificial Intelligence Research* 80:1623–1701.

McCann RJ (1997) A convexity principle for interacting gases. *Advances in Mathematics* 128(1):153–179.

Qi M, Grigas P, Shen ZJM (2025) Integrated conditional estimation-optimization. *Operations Research* 0(0):null, URL <http://dx.doi.org/10.1287/opre.2023.0427>.

Sadana U, Chenreddy A, Delage E, Forel A, Frejinger E, Vidal T (2025) A survey of contextual optimization methods for decision-making under uncertainty. *European Journal of Operational Research* 320(2):271–289.

Zhu T, Xie J, Sim M (2022) Joint estimation and robustness optimization. *Management Science* 68(3):1659–1677.

Appendix A: LP Formulation for DF Optimal Transport under Empirical Distribution

Let

$$\hat{\mu}_{n_\mu} := \sum_{i=1}^{n_\mu} a_i \delta_{x_i}, \quad \hat{\nu}_{n_\nu} := \sum_{j=1}^{n_\nu} b_j \delta_{y_j},$$

where $a_i \geq 0$, $b_j \geq 0$, $\sum_i a_i = \sum_j b_j = 1$ (uniform weights correspond to $a_i = 1/n_\mu$ and $b_j = 1/n_\nu$). Any coupling between $\hat{\mu}_{n_\mu}$ and $\hat{\nu}_{n_\nu}$ can be identified with a nonnegative matrix $\Pi \in \mathbb{R}_+^{n_\mu \times n_\nu}$ whose row and column sums match $a := (a_i)$ and $b := (b_j)$. The empirical optimistic and robust DF distances are therefore

$$\begin{aligned} W_{\text{DF}}^{\text{O}}(\hat{\mu}_{n_\mu}, \hat{\nu}_{n_\nu}) &= \min_{\Pi \geq 0} \sum_{i=1}^{n_\mu} \sum_{j=1}^{n_\nu} \ell_{\text{SPO}}(x_i, y_j) \Pi_{ij} \quad \text{s.t.} \quad \Pi \mathbf{1} = b, \quad \Pi^\top \mathbf{1} = a, \\ W_{\text{DF}}^{\text{R}}(\hat{\mu}_{n_\mu}, \hat{\nu}_{n_\nu}) &= \max_{\Pi \geq 0} \sum_{i=1}^{n_\mu} \sum_{j=1}^{n_\nu} \ell_{\text{SPO}}(x_i, y_j) \Pi_{ij} \quad \text{s.t.} \quad \Pi \mathbf{1} = b, \quad \Pi^\top \mathbf{1} = a. \end{aligned}$$

Solving the above two LPs for calculating the W_{DF}^{O} and W_{DF}^{R} is generally tractable, when the sample sizes n_ν and n_μ are small. When they are large or when μ and ν are continuous, we instead use the method in Section 4.

Appendix B: Motivation for the Robust DF Distance: Opportunism Robustness

The Robust DF distance in Definition 2 can be interpreted through the lens of robust decision-making under uncertainty about how a proxy cost vector relates to the true one. To see this, consider an uncertainty set $\mathcal{U} \subset \mathbb{R}^d$ that contains all plausible realizations of a cost vector. Suppose a decision-maker observes (or predicts) a proxy $x \in \mathcal{U}$ and implements the downstream decision $w^*(x)$, but the realized (true) cost is some $y \in \mathcal{U}$. A natural robustness objective is to choose x so as to minimize the worst-case decision degradation measured by the SPO loss:

$$\min_{x \in \mathcal{U}} \max_{y \in \mathcal{U}} \ell_{\text{SPO}}(x, y) = \min_{x \in \mathcal{U}} \max_{y \in \mathcal{U}} (y^\top w^*(x) - y^\top w^*(y)). \quad (23)$$

This is a predict-then-optimize analogue of classical robust optimization: we do not directly choose $w \in S$, but rather choose a proxy x that determines the implemented decision $w^*(x)$, and we evaluate it against the worst-case true cost y .

In stochastic settings, the uncertainty-set viewpoint is naturally replaced by distributional information. Here, μ and ν represent the marginal laws of the proxy X and the true vector Y , respectively, but the *dependence* between X and Y may be unknown or misspecified. In such cases, it is reasonable to guard against opportunistic (overly favorable) dependence assumptions by considering the worst-case alignment of outcomes drawn from μ and ν . Since $\Gamma(\mu, \nu)$ is precisely the set of all joint laws consistent with these marginals, the robust DF distance

$$W_{\text{DF}}^{\text{R}}(\mu, \nu) = \sup_{\gamma \in \Gamma(\mu, \nu)} W_{\text{SPO}}(\mu, \nu; \gamma) = \sup_{\gamma \in \Gamma(\mu, \nu)} \mathbb{E}_\gamma [\ell_{\text{SPO}}(X, Y)]$$

can be viewed as a distributional analogue of (23). In this analogy, the “decision” is a randomized policy represented by the proxy distribution μ : rather than choosing a single proxy x , the decision-maker commits to a distribution over proxy cost vectors, observes a realization $X \sim \mu$, and implements the induced decision $w^*(X)$.

Under this interpretation, the coupling $\gamma \in \Gamma(\mu, \nu)$ plays the role of an adversary. After the decision-maker fixes the proxy marginal μ (and the true marginal ν is given), the adversary selects a dependence structure between $X \sim \mu$ and $Y \sim \nu$, i.e., a joint law γ with these marginals, to maximize the expected SPO loss. The robust DF distance

$$W_{\text{DF}}^R(\mu, \nu) = \sup_{\gamma \in \Gamma(\mu, \nu)} \mathbb{E}_\gamma [\ell_{\text{SPO}}(X, Y)]$$

therefore quantifies the worst-case expected decision degradation over all joint distributions consistent with the given marginals.

Thus, $W_{\text{DF}}^R(\mu, \nu)$ is a distributional analogue of (23): the pointwise maximization over $y \in \mathcal{U}$ is replaced by a maximization over couplings $\gamma \in \Gamma(\mu, \nu)$, and the deterministic proxy choice x is replaced by a randomized proxy $X \sim \mu$. Moreover, if the decision-maker is allowed to choose the proxy marginal within a class of distributions \mathcal{M} , then minimizing the robust DF distance,

$$\inf_{\mu \in \mathcal{M}} W_{\text{DF}}^R(\mu, \nu),$$

amounts to selecting a proxy distribution that minimizes the worst-case expected SPO loss over all couplings consistent with (μ, ν) .

Appendix C: McCann interpolation via the W_2 reduction

In this Appendix, we provide another method to construct the interpolation via the W_2 reduction in the space $\Gamma(w^* \# \mu_0, \mu_1)$. Unlike the quadratic optimal transport setting, the SPO transport cost $\ell_{\text{SPO}}(x, y)$ is not induced by a quadratic metric (and can be discontinuous due to the piecewise-constant oracle w^*). As a result, the classical geodesic/convexity properties of McCann interpolation for W_2 do not automatically extend to the decision-focused interpolants in Section 5.2.

For the *optimistic* DF distance, however, Theorems 1–2 imply a reduction to quadratic transport after pushing μ forward through the oracle map. Recall $w^*(\cdot)$ from (4) and define

$$\bar{w}^*(x) := -w^*(x), \quad \alpha := (\bar{w}^*)_\# \mu.$$

Given any coupling $\gamma \in \Gamma(\mu, \nu)$, let

$$\eta := (\bar{w}^* \times \text{Id})_\# \gamma \in \Gamma(\alpha, \nu).$$

Since $\ell_{\text{SPO}}(x, y) = y^\top w^*(x) - y^\top w^*(y) = -y^\top \bar{w}^*(x) - y^\top w^*(y)$ and $-a^\top y = \frac{1}{2}(\|a - y\|_2^2 - \|a\|_2^2 - \|y\|_2^2)$, we obtain the decomposition

$$\int \ell_{\text{SPO}}(x, y) \gamma(dx, dy) = \frac{1}{2} \int \|a - y\|_2^2 \eta(da, dy) + C(\mu, \nu), \quad (24)$$

where $C(\mu, \nu)$ depends only on the marginals (hence is independent of the coupling). Consequently,

$$W_{\text{DF}}^0(\mu, \nu) = \inf_{\eta \in \Gamma(\alpha, \nu)} \frac{1}{2} \int \|a - y\|_2^2 \eta(da, dy) + C(\mu, \nu) = \frac{1}{2} W_2^2(\alpha, \nu) + C(\mu, \nu). \quad (25)$$

This reduction suggests defining a standard McCann displacement interpolation in the reduced (decision) space between α and ν , and then *lifting* it back to couplings whose first marginal is μ .

PROPOSITION 6 (McCann geodesic in decision space and consistent lifts). *Let $\mu, \nu \in \mathcal{P}_2(\mathbb{R}^d)$ and define $\bar{w}^*(x) := -w^*(x)$ and $\alpha := (\bar{w}^*)_\# \mu$. Let $\eta^* \in \Gamma(\alpha, \nu)$ be an optimal coupling for the quadratic cost, i.e.,*

$$\eta^* \in \arg \min_{\eta \in \Gamma(\alpha, \nu)} \int_{\mathbb{R}^d \times \mathbb{R}^d} \|a - y\|_2^2 \eta(da, dy).$$

For $t \in [0, 1]$ define $\pi_t(a, y) = (1 - t)a + ty$ and set

$$\nu_t := (\pi_t)_\# \eta^*, \quad \eta_t := (\text{Id}, \pi_t)_\# \eta^* \in \Gamma(\alpha, \nu_t).$$

Let $\{w_k\}_{k=1}^K$ be the extreme points of S and define the (measurable) decision regions

$$C_k := \{x \in \mathbb{R}^d : w^*(x) = w_k\}, \quad k = 1, \dots, K,$$

which form a partition of \mathbb{R}^d up to boundaries. Then α is supported on $\{-w_k\}_{k=1}^K$ and satisfies $\alpha(\{-w_k\}) = \mu(C_k)$.

For each $t \in [0, 1]$, define a lifted coupling γ_t between μ and ν_t by

$$\gamma_t(A, B) := \sum_{k=1}^K \frac{\mu(A \cap C_k)}{\mu(C_k)} \eta_t(\{-w_k\} \times B), \quad A, B \subseteq \mathbb{R}^d \text{ measurable}, \quad (26)$$

with the convention that terms with $\mu(C_k) = 0$ are omitted. Then:

1. **(McCann geodesic / constant speed in the reduced space).** The curve $\{\nu_t\}_{t \in [0, 1]}$ is the McCann displacement interpolation between α and ν ; in particular,

$$W_2(\nu_s, \nu_t) = |t - s| W_2(\alpha, \nu), \quad \forall s, t \in [0, 1].$$

2. **(Displacement identities).** If $(A, Y) \sim \eta^*$ and $Y_t = (1 - t)A + tY$, then for all $s, t \in [0, 1]$,

$$\mathbb{E}\|Y_t - A\|_2^2 = t^2 W_2^2(\alpha, \nu), \quad \mathbb{E}\|Y_t - Y_s\|_2^2 = (t - s)^2 W_2^2(\alpha, \nu).$$

3. **(Lift consistency).** For each $t \in [0, 1]$, the measure γ_t defined in (26) is a coupling in $\Gamma(\mu, \nu_t)$ and satisfies the push-forward identity

$$(\bar{w}^* \times \text{Id})_\# \gamma_t = \eta_t.$$

In particular, $(\bar{w}^* \times \text{Id})_\# \gamma_1 = \eta^*$.

4. **(Per-time optimality for the optimistic DF distance).** Fix $t \in [0, 1]$. If $\tilde{\eta}_t$ is any optimal coupling for the quadratic cost between α and ν_t , then the lift $\tilde{\gamma}_t$ defined by (26) with η_t replaced by $\tilde{\eta}_t$ is optimal for $W_{\text{DF}}^0(\mu, \nu_t)$, i.e.,

$$\int \ell_{\text{SPO}}(x, y) \tilde{\gamma}_t(dx, dy) = \inf_{\gamma \in \Gamma(\mu, \nu_t)} \int \ell_{\text{SPO}}(x, y) \gamma(dx, dy).$$

In particular, the lifted couplings obtained from the McCann plan η_t provide a canonical family of DF-optimal couplings between μ and ν_t .

Proof of Proposition 6 (1)–(2). These are standard consequences of quadratic optimal transport. If $(A, Y) \sim \eta^*$ and $Y_t = (1-t)A + tY$, then $\nu_t := (Y_t)_\# \mathbb{P}$ is the McCann displacement interpolation between α and ν , yielding the constant-speed identity. Moreover, $Y_t - A = t(Y - A)$ and $Y_t - Y_s = (t-s)(Y - A)$, so the stated second-moment formulas follow from $\mathbb{E}\|Y - A\|_2^2 = W_2^2(\alpha, \nu)$.

(3). We first verify that $\gamma_t \in \Gamma(\mu, \nu_t)$. For any measurable $A \subseteq \mathbb{R}^d$,

$$\begin{aligned} \gamma_t(A, \mathbb{R}^d) &= \sum_{k: \mu(C_k) > 0} \frac{\mu(A \cap C_k)}{\mu(C_k)} \eta_t(\{-w_k\} \times \mathbb{R}^d) \\ &= \sum_{k: \mu(C_k) > 0} \frac{\mu(A \cap C_k)}{\mu(C_k)} \alpha(\{-w_k\}) \\ &= \sum_{k=1}^K \mu(A \cap C_k) \\ &= \mu(A), \end{aligned}$$

since η_t has first marginal α and $\alpha(\{-w_k\}) = \mu(C_k)$. Similarly, for any measurable $B \subseteq \mathbb{R}^d$,

$$\gamma_t(\mathbb{R}^d, B) = \sum_{k: \mu(C_k) > 0} \eta_t(\{-w_k\} \times B) = \eta_t(\mathbb{R}^d \times B) = \nu_t(B),$$

so the second marginal is ν_t .

For the push-forward identity, note that $\bar{w}^*(x) = -w_k$ for $x \in C_k$. Thus, for any measurable $B \subseteq \mathbb{R}^d$,

$$((\bar{w}^* \times \text{Id})_\# \gamma_t)(\{-w_k\} \times B) = \gamma_t(C_k, B) = \eta_t(\{-w_k\} \times B),$$

which implies $(\bar{w}^* \times \text{Id})_\# \gamma_t = \eta_t$.

(4). Fix $t \in [0, 1]$ and let $\tilde{\eta}_t$ be optimal for the quadratic cost between α and ν_t . Let $\tilde{\gamma}_t$ be its lift as in (26). By part (3), $(\bar{w}^* \times \text{Id})_\# \tilde{\gamma}_t = \tilde{\eta}_t$. Using the reduction identity (24) with ν replaced by ν_t , we obtain for any $\gamma \in \Gamma(\mu, \nu_t)$ and $\eta = (\bar{w}^* \times \text{Id})_\# \gamma \in \Gamma(\alpha, \nu_t)$,

$$\int \ell_{\text{SPO}}(x, y) \gamma(dx, dy) = \frac{1}{2} \int \|a - y\|_2^2 \eta(da, dy) + C(\mu, \nu_t),$$

where $C(\mu, \nu_t)$ does not depend on the coupling. Minimizing the left-hand side over $\Gamma(\mu, \nu_t)$ is therefore equivalent to minimizing the quadratic cost over $\Gamma(\alpha, \nu_t)$, and the lift $\tilde{\gamma}_t$ attains this minimum. This proves the claimed optimality of $\tilde{\gamma}_t$ for $W_{\text{DF}}^0(\mu, \nu_t)$.

Discussion and comparison with the coupling-driven interpolant. Proposition 6 provides four complementary statements that clarify what is preserved (and what is not) when one constructs an interpolation path via the W_2 reduction. We discuss each item and compare it with Theorem 4, which analyzes the direct coupling-driven interpolant $\nu_t = (\pi_t)_\# \gamma^*$ built from an optimizer of $W_{\text{DF}}^0(\mu, \nu)$ in the original data space.

(1) Constant speed, but in the reduced (decision) space. Item (1) states that $\{\nu_t\}_{t \in [0, 1]}$ is a genuine constant-speed W_2 geodesic between α and ν , namely $W_2(\nu_s, \nu_t) = |t - s| W_2(\alpha, \nu)$. This is a *stronger and two-sided* statement than the one-sided bound in Theorem 4, but it applies to the reduced-space geometry induced by the quadratic cost. In contrast, Theorem 4 controls the growth of the optimistic DF distance along a path that is defined directly by a DF-optimal coupling in the original space, without requiring any W_2 structure.

(2) Quadratic energy identities along the path. Item (2) records exact second-moment identities along the displacement interpolation. These identities are a hallmark of quadratic OT and are useful for quantifying the “energy” of the path and for deriving stability bounds. No analogue of these exact equalities is expected for the coupling-driven DF interpolant in Theorem 4, because ℓ_{SPO} is generally non-quadratic and the oracle map w^* induces piecewise-constant discontinuities.

(3) A canonical lift back to the data space. Item (3) constructs a family of couplings $\gamma_t \in \Gamma(\mu, \nu_t)$ that are consistent with the reduced-space plan in the sense that $(\bar{w}^* \times \text{Id})_\# \gamma_t = \eta_t$. This lift makes explicit how to relate the reduced-space interpolation to the original decision-focused problem: the path $\{\nu_t\}$ is generated in the reduced space, but the corresponding couplings with the original marginal μ are recovered by conditioning on the decision regions $\{C_k\}$. Theorem 4 does not provide such a lift because it starts from a data-space DF-optimal coupling γ^* directly, and then pushes it forward without changing the first marginal.

(4) Per-time optimality for $W_{\text{DF}}^{\text{O}}(\mu, \nu_t)$. Perhaps most importantly, Item (4) shows that for each fixed t , one can choose a quadratic-optimal coupling between α and ν_t and lift it to obtain a coupling that is *optimal for* $W_{\text{DF}}^{\text{O}}(\mu, \nu_t)$. This is a per-time optimality statement: at each intermediate marginal ν_t , the construction yields a DF-optimal coupling between μ and ν_t . In comparison, Theorem 4 guarantees only the one-sided bound $W_{\text{DF}}^{\text{O}}(\mu, \nu_t) \leq t W_{\text{DF}}^{\text{O}}(\mu, \nu)$ along the interpolant induced by a *single* DF-optimal coupling between μ and ν ; it does not assert that the pushed-forward coupling remains optimal for the intermediate problems (μ, ν_t) . In general, such dynamic optimality need not hold for non-quadratic costs.

Theorem 4 applies to a broad class of decision-focused costs and yields a simple, coupling-driven path with a monotone (one-sided) distance control based only on concavity of the value function. Proposition 6, in contrast, leverages the W_2 reduction available for the optimistic DF distance to recover several *exact* quadratic-OT properties (constant speed, energy identities) and a stronger notion of intermediate-time optimality via lifting. The two approaches are therefore complementary: the direct interpolant is more intrinsic to the DF objective, while the reduced-space McCann construction provides sharper structure when the quadratic reduction applies.

Appendix D: Omitted Proof

Proof of Proposition 1 Let γ be the joint law of $(X, Y) = (X, \kappa X)$; then $\gamma \in \Gamma(\mu, \nu)$. For any realization, if $\kappa > 0$ then

$$\arg \min_{w \in S} w^\top (\kappa X) = \arg \min_{w \in S} \kappa w^\top X = \arg \min_{w \in S} w^\top X,$$

so by the scale-invariance of the oracle selection we have $w^*(Y) = w^*(X)$. If $\kappa = 0$, then $Y = 0$ and $\ell_{\text{SPO}}(X, Y) = 0^\top w^*(X) - 0^\top w^*(0) = 0$. Hence $\ell_{\text{SPO}}(X, Y) = 0$ almost surely, and therefore $W_{\text{SPO}}(\mu, \nu; \gamma) = \mathbb{E}[\ell_{\text{SPO}}(X, Y)] = 0$.

Finally, $\ell_{\text{SPO}}(x, y) \geq 0$ for all x, y because $w^*(y)$ minimizes $y^\top w$ over S , implying $y^\top w^*(y) \leq y^\top w^*(x)$. Taking the infimum over $\Gamma(\mu, \nu)$ yields $W_{\text{DF}}^{\text{O}}(\mu, \nu) = 0$. \square

Proof of Proposition 2 The inequality $W_{\text{DF}}^{\text{O}}(\mu, \nu) \leq W_{\text{sym}}^{\text{O}}(\mu, \nu)$ is immediate since $W_{\text{sym}}^{\text{O}}(\mu, \nu) = W_{\text{DF}}^{\text{O}}(\mu, \nu) + W_{\text{DF}}^{\text{O}}(\nu, \mu)$ and $W_{\text{DF}}^{\text{O}}(\nu, \mu) \geq 0$.

To bound $W_{\text{sym}}^{\text{O}}$, fix any coupling $\gamma \in \Gamma(\mu, \nu)$ and let γ^\top denote its transpose. By feasibility of γ and γ^\top ,

$$W_{\text{DF}}^{\text{O}}(\mu, \nu) \leq \int \ell_{\text{SPO}}(x, y) \gamma(dx, dy) \quad \text{and} \quad W_{\text{DF}}^{\text{O}}(\nu, \mu) \leq \int \ell_{\text{SPO}}(x, y) \gamma^\top(dx, dy) = \int \ell_{\text{SPO}}(y, x) \gamma(dx, dy).$$

Adding the two inequalities and using $\ell_{\text{SPO}}(x, y) + \ell_{\text{SPO}}(y, x) = (x - y)^\top (w^*(y) - w^*(x))$, we obtain

$$W_{\text{sym}}^{\text{O}}(\mu, \nu) \leq \int (x - y)^\top (w^*(y) - w^*(x)) \gamma(dx, dy) \leq \int \|x - y\|_2 \|w^*(y) - w^*(x)\|_2 \gamma(dx, dy).$$

Since $w^*(x), w^*(y) \in S$, we have $\|w^*(y) - w^*(x)\|_2 \leq D_W$, and therefore

$$W_{\text{sym}}^O(\mu, \nu) \leq D_W \int \|x - y\|_2 \gamma(dx, dy).$$

Taking the infimum over $\gamma \in \Gamma(\mu, \nu)$ yields $W_{\text{sym}}^O(\mu, \nu) \leq D_W W_1(\mu, \nu)$.

Finally, on a bounded set \mathcal{Y} we have the elementary bound $W_1(\mu, \nu) \leq \|\mathcal{Y}\| d_{\text{TV}}(\mu, \nu)$. Combining this with Pinsker's inequality $d_{\text{TV}}(\mu, \nu) \leq \sqrt{\frac{1}{2} \text{KL}(\mu\|\nu)}$ (when $\text{KL}(\mu\|\nu) < \infty$) gives the stated KL control. \square

Proof of Proposition 3 By definition,

$$W_{\text{DF}}^O(\mu, \nu) = \inf_{\gamma \in \Gamma(\mu, \nu)} \int y^\top (w^*(x) - w^*(y)) d\gamma(x, y).$$

Applying Cauchy–Schwarz to the integrand yields

$$W_{\text{DF}}^O(\mu, \nu) \leq \inf_{\gamma \in \Gamma(\mu, \nu)} \left(\int \|y\|_2^2 d\gamma(x, y) \right)^{1/2} \left(\int \|w^*(x) - w^*(y)\|_2^2 d\gamma(x, y) \right)^{1/2}.$$

The first factor depends only on the second marginal of γ , hence

$$\left(\int \|y\|_2^2 d\gamma(x, y) \right)^{1/2} = \left(\int \|y\|_2^2 d\nu(y) \right)^{1/2} =: V.$$

To handle the second factor, push any $\gamma \in \Gamma(\mu, \nu)$ forward through the oracle map in both coordinates. Specifically, let $\tilde{\gamma} := (w^* \times w^*)_\# \gamma$. Then $\tilde{\gamma} \in \Gamma(w_\#^* \mu, w_\#^* \nu)$ and

$$\int \|w^*(x) - w^*(y)\|_2^2 d\gamma(x, y) = \int \|u - v\|_2^2 d\tilde{\gamma}(u, v).$$

Conversely, given any $\tilde{\gamma} \in \Gamma(w_\#^* \mu, w_\#^* \nu)$, one can construct a coupling $\gamma \in \Gamma(\mu, \nu)$ whose oracle-level push-forward equals $\tilde{\gamma}$ by sampling $(U, V) \sim \tilde{\gamma}$ and then, conditional on $(U, V) = (w_i, w_j)$, sampling $X \sim \mu(\cdot | D_i)$ and $Y \sim \nu(\cdot | D_j)$.

This construction ensures $(w^*(X), w^*(Y)) \sim \tilde{\gamma}$ and preserves the above quadratic cost identity. Therefore,

$$\left(\inf_{\gamma \in \Gamma(\mu, \nu)} \int \|w^*(x) - w^*(y)\|_2^2 d\gamma(x, y) \right)^{1/2} = W_2(w_\#^* \mu, w_\#^* \nu). \quad (27)$$

Combining the pieces gives $W_{\text{DF}}^O(\mu, \nu) \leq V W_2(w_\#^* \mu, w_\#^* \nu)$.

To upper bound $W_2(w_\#^* \mu, w_\#^* \nu)$ in terms of d_{TV} , match the common mass at each atom w_i at zero cost, and transport the remaining mass (of total size $d_{\text{TV}}(w_\#^* \mu, w_\#^* \nu)$) within S at cost at most D_W^2 per unit. This yields

$$W_2^2(w_\#^* \mu, w_\#^* \nu) \leq D_W^2 d_{\text{TV}}(w_\#^* \mu, w_\#^* \nu), \quad \text{hence} \quad W_2(w_\#^* \mu, w_\#^* \nu) \leq D_W \sqrt{d_{\text{TV}}(w_\#^* \mu, w_\#^* \nu)}.$$

Finally, Pinsker's inequality $d_{\text{TV}}(P, Q) \leq \sqrt{\frac{1}{2} \text{KL}(P\|Q)}$ gives the KL control. \square

Proof of Proposition 4 Fix $0 \leq \varepsilon < \varepsilon'$ and any $\gamma \in \Gamma(\mu, \nu)$. Since $\text{KL}(\gamma \parallel \mu \otimes \nu) \geq 0$,

$$\int \ell_{\text{SPO}}(x, y) d\gamma(x, y) + \varepsilon' \text{KL}(\gamma \parallel \mu \otimes \nu) \geq \int \ell_{\text{SPO}}(x, y) d\gamma(x, y) + \varepsilon \text{KL}(\gamma \parallel \mu \otimes \nu).$$

Taking the infimum over $\gamma \in \Gamma(\mu, \nu)$ shows that $W_{\text{DF}}^{\text{ER-O}}(\mu, \nu; \varepsilon') \geq W_{\text{DF}}^{\text{ER-O}}(\mu, \nu; \varepsilon)$. The monotonicity of $W_{\text{DF}}^{\text{ER-R}}$ follows similarly since the regularization term enters with a minus sign in (E-DFR).

For the bounds, note first that $W_{\text{DF}}^{\text{ER-O}}(\mu, \nu; 0) = W_{\text{DF}}^{\text{O}}(\mu, \nu)$ and $W_{\text{DF}}^{\text{ER-R}}(\mu, \nu; 0) = W_{\text{DF}}^{\text{R}}(\mu, \nu)$. Since the KL term is nonnegative, we also have $W_{\text{DF}}^{\text{ER-O}}(\mu, \nu; \varepsilon) \geq W_{\text{DF}}^{\text{O}}(\mu, \nu)$ for all $\varepsilon \geq 0$. On the other hand, choosing the independent coupling $\gamma = \mu \otimes \nu$ (for which $\text{KL}(\gamma \parallel \mu \otimes \nu) = 0$) in (E-DFO) yields

$$W_{\text{DF}}^{\text{ER-O}}(\mu, \nu; \varepsilon) \leq \int \ell_{\text{SPO}}(x, y) (\mu \otimes \nu)(dx, dy) = R(\mu, \nu).$$

This proves $W_{\text{DF}}^{\text{O}}(\mu, \nu) \leq W_{\text{DF}}^{\text{ER-O}}(\mu, \nu; \varepsilon) \leq R(\mu, \nu)$.

Similarly, for (E-DFR), we have

$$W_{\text{DF}}^{\text{ER-R}}(\mu, \nu; \varepsilon) \leq \sup_{\gamma \in \Gamma(\mu, \nu)} \int \ell_{\text{SPO}}(x, y) d\gamma(x, y) = W_{\text{DF}}^{\text{R}}(\mu, \nu),$$

and again evaluating (E-DFR) at $\gamma = \mu \otimes \nu$ gives $W_{\text{DF}}^{\text{ER-R}}(\mu, \nu; \varepsilon) \geq R(\mu, \nu)$. This completes the proof. \square

Proof of Lemma 1 Let $\mathfrak{f} : \mathbb{R}^d \times \mathbb{R}^d \rightarrow S \times \mathbb{R}^d$ be $\mathfrak{f}(x, y) := (w^*(x), y)$. For any $\gamma \in \Gamma(\mu, \nu)$, the push-forward $\bar{\gamma} := \mathfrak{f}_\# \gamma$ satisfies $\bar{\gamma} \in \Gamma(w^*_\# \mu, \nu)$, and by the change-of-variables formula,

$$\int h(y)^\top w^*(x) d\gamma(x, y) = \int h(y)^\top w d\bar{\gamma}(w, y).$$

Taking infima over γ gives

$$\inf_{\gamma \in \Gamma(\mu, \nu)} \int h(y)^\top w^*(x) d\gamma(x, y) \geq \inf_{\bar{\gamma} \in \Gamma(w^*_\# \mu, \nu)} \int h(y)^\top w d\bar{\gamma}(w, y).$$

For the reverse inequality, write $w^*(x) = \sum_{i=1}^{|\mathfrak{S}|} w_i \mathbf{1}_{D_i}(x)$, where $\mathfrak{S} = \{w_1, \dots, w_{|\mathfrak{S}|}\}$ is the set of extreme points of S and $D_i := \{x : w^*(x) = w_i\}$. Fix any $\bar{\gamma} \in \Gamma(w^*_\# \mu, \nu)$ and define a measure γ on measurable rectangles by

$$\gamma(A, B) := \sum_{i=1}^{|\mathfrak{S}|} \mu(A \cap D_i) \frac{\bar{\gamma}(\{w_i\} \times B)}{\mu(D_i)}, \quad A, B \in \mathcal{B}(\mathbb{R}^d), \quad (28)$$

with the convention that the i th term is 0 when $\mu(D_i) = 0$. The definition (28) extends (by linearity and standard measure arguments) to a coupling $\gamma \in \Gamma(\mu, \nu)$ and satisfies $\mathfrak{f}_\# \gamma = \bar{\gamma}$. Consequently,

$$\int h(y)^\top w^*(x) d\gamma(x, y) = \int h(y)^\top w d\bar{\gamma}(w, y),$$

and taking infima over $\bar{\gamma}$ yields the desired \leq inequality. Combining the two directions proves the claim. \square

Proof of Theorem 2 First, γ is well-defined by (8). For any measurable A ,

$$\gamma(A, \mathbb{R}^d) = \sum_{k=1}^{|\mathfrak{S}|} \mu(A \cap D_k) \frac{\gamma^*(\{-w_k\} \times \mathbb{R}^d)}{\mu(D_k)} = \sum_{k=1}^{|\mathfrak{S}|} \mu(A \cap D_k) = \mu(A),$$

since γ^* has first marginal $(\bar{w}^*)_\# \mu$ and $(\bar{w}^*)_\# \mu(\{-w_k\}) = \mu(D_k)$. Likewise, for any measurable B ,

$$\gamma(\mathbb{R}^d, B) = \sum_{k=1}^{|\mathfrak{S}|} \mu(D_k) \frac{\gamma^*(\{-w_k\} \times B)}{\mu(D_k)} = \sum_{k=1}^{|\mathfrak{S}|} \gamma^*(\{-w_k\} \times B) = \nu(B),$$

so $\gamma \in \Gamma(\mu, \nu)$.

Next, by construction, pushing γ forward through $\mathfrak{f}(x, y) = (\bar{w}^*(x), y)$ recovers γ^* , i.e., $\mathfrak{f}_\# \gamma = \gamma^*$. In the proof of Theorem 1, we showed that for any $\gamma \in \Gamma(\mu, \nu)$, the value $W_{\text{SPO}}(\mu, \nu; \gamma)$ equals a constant (depending only on $(\bar{w}^*)_\# \mu$ and ν) plus $\frac{1}{2} \int \|w - y\|_2^2 d(\mathfrak{f}_\# \gamma)(w, y)$. Therefore, choosing γ so that $\mathfrak{f}_\# \gamma = \gamma^*$ and using optimality of γ^* for the quadratic cost yields $W_{\text{SPO}}(\mu, \nu; \gamma) = W_{\text{DF}}^0(\mu, \nu)$. \square

Proof of Proposition 5 By Definition 2 and $\ell_{\text{SPO}}(x, y) = y^\top w^*(x) - y^\top w^*(y)$,

$$W_{\text{DF}}^0(\mu, \nu) = \inf_{\gamma \in \Gamma(\mu, \nu)} \int_{\mathbb{R}^d \times \mathbb{R}^d} (y^\top w^*(x) - z(y)) d\gamma(x, y).$$

Applying Lemma 1 with $h(y) = y$ yields the reduction

$$W_{\text{DF}}^0(\mu, \nu) = \inf_{\bar{\gamma} \in \Gamma(w^*_\# \mu, \nu)} \int_{\mathfrak{S} \times \mathbb{R}^d} (y^\top w - z(y)) d\bar{\gamma}(w, y).$$

Since $w^*_\# \mu$ is supported on the finite set \mathfrak{S} , we may write $w^*_\# \mu = \sum_{i=1}^{|\mathfrak{S}|} \mu(D_i) \delta_{w_i}$, and the above becomes an optimal transport problem between the discrete measure $w^*_\# \mu$ and ν with cost $c(w_i, y) = c_i(y)$.

The Kantorovich duality theorem for optimal transport (which applies here since the first space is finite and the cost is measurable and integrable) gives

$$\inf_{\bar{\gamma} \in \Gamma(w^*_\# \mu, \nu)} \int c(w, y) d\bar{\gamma}(w, y) = \sup_{\varphi, \psi} \left\{ \int \varphi(w) d(w^*_\# \mu)(w) + \int \psi(y) d\nu(y) : \varphi(w) + \psi(y) \leq c(w, y) \right\},$$

where φ is a function on \mathfrak{S} and $\psi \in L^1(\nu)$. Identifying $\varphi(w_i)$ with f_i and ψ with g yields exactly (11)–(10).

Finally, for any fixed f , the constraint (10) implies $g(y) \leq \min_i (c_i(y) - f_i)$ pointwise. Since the objective in (11) is increasing in g , the best feasible choice is $g = g_f$ as defined in (12), which gives (13). \square

Proof of Theorem 4 Let $\text{Id} : \mathbb{R}^d \rightarrow \mathbb{R}^d$ denote the identity map, and define the coupling $\gamma_t^* := (\text{Id}, \pi_t)_\# \gamma^* \in \Gamma(\mu, \nu_t)$.

By definition,

$$W_{\text{DF}}^0(\mu, \nu_t) = \inf_{\gamma \in \Gamma(\mu, \nu_t)} \int \ell_{\text{SPO}}(u, w) d\gamma(u, w).$$

Since $\gamma_t^* := (\text{Id}, \pi_t)_\# \gamma^* \in \Gamma(\mu, \nu_t)$ is feasible, we have

$$W_{\text{DF}}^0(\mu, \nu_t) \leq \int \ell_{\text{SPO}}(u, w) d\gamma_t^*(u, w). \quad (29)$$

By the push-forward identity, for any measurable function φ ,

$$\int \varphi(u, w) d(\text{Id}, \pi_t)_\# \gamma^*(u, w) = \int \varphi(u, \pi_t(u, v)) d\gamma^*(u, v).$$

Applying this with $\varphi(u, w) = \ell_{\text{SPO}}(u, w)$ yields

$$\int \ell_{\text{SPO}}(u, w) d\gamma_t^*(u, w) = \int \ell_{\text{SPO}}(u, \pi_t(u, v)) d\gamma^*(u, v). \quad (30)$$

Combining (29) and (30) proves the first inequality in the theorem,

$$W_{\text{DF}}^0(\mu, \nu_t) \leq \int \ell_{\text{SPO}}(u, \pi_t(u, v)) d\gamma^*(u, v).$$

Define the value function $z(x) := \min_{w \in S} w^\top x$, so $z(x) = x^\top w^*(x)$. Using $\ell_{\text{SPO}}(u, y) = y^\top w^*(u) - z(y)$ and $\pi_t(u, v) = (1-t)u + tv$, we obtain

$$\begin{aligned} \ell_{\text{SPO}}(u, \pi_t(u, v)) &= ((1-t)u + tv)^\top w^*(u) - z((1-t)u + tv) \\ &= (1-t) u^\top w^*(u) + t v^\top w^*(u) - z((1-t)u + tv) \\ &= (1-t) z(u) + t v^\top w^*(u) - z((1-t)u + tv). \end{aligned} \quad (31)$$

Since $z(x) = \min_{w \in S} w^\top x$ is the pointwise minimum of linear functions, z is concave. Hence, for all u, v and $t \in [0, 1]$,

$$z((1-t)u + tv) \geq (1-t) z(u) + t z(v). \quad (32)$$

Substituting (32) into (31) yields

$$\begin{aligned} \ell_{\text{SPO}}(u, \pi_t(u, v)) &\leq (1-t) z(u) + t v^\top w^*(u) - ((1-t) z(u) + t z(v)) \\ &= t(v^\top w^*(u) - z(v)) \\ &= t \ell_{\text{SPO}}(u, v). \end{aligned} \quad (33)$$

Integrating (33) with respect to γ^* gives

$$\int \ell_{\text{SPO}}(u, \pi_t(u, v)) d\gamma^*(u, v) \leq t \int \ell_{\text{SPO}}(u, v) d\gamma^*(u, v). \quad (34)$$

Since γ^* is an optimizer for $W_{\text{DF}}^0(\mu, \nu)$,

$$\int \ell_{\text{SPO}}(u, v) d\gamma^*(u, v) = W_{\text{DF}}^0(\mu, \nu). \quad (35)$$

Combining (34) and (35) yields

$$\int \ell_{\text{SPO}}(u, \pi_t(u, v)) d\gamma^*(u, v) \leq t W_{\text{DF}}^{\text{O}}(\mu, \nu).$$

Putting together Step 1–Step 5, we obtain

$$W_{\text{DF}}^{\text{O}}(\mu, \nu_t) \leq \int \ell_{\text{SPO}}(u, \pi_t(u, v)) d\gamma^*(u, v) \leq t W_{\text{DF}}^{\text{O}}(\mu, \nu),$$

and in particular $W_{\text{DF}}^{\text{O}}(\mu, \nu_t) \leq t W_{\text{DF}}^{\text{O}}(\mu, \nu)$. \square

Appendix E: Details for Numerical Study

E.0.1. Dataset and preprocessing

Dataset. We use the *Parkinson’s Telemonitoring* dataset (UCI repository), which contains 5,875 total observations from 42 Parkinson’s disease patients (unique `subject#`). Each observation includes a measurement time `test_time` (days from study start), two clinical severity measures `motor_UPDRS` and `total_UPDRS`, and multiple voice-related features. The data are longitudinal: the same patient is measured repeatedly over time, which enables both population-level distribution comparisons and patient-tracked evaluations.

Time snapshots via windowing. Because measurements occur at irregular times, we approximate three “snapshots” of the population distribution at days $t \in \{50, 100, 150\}$ by using an integer-rounded time and a symmetric window of width ± 5 days. Concretely, we define

$$\mathcal{D}_t := \{\text{observations with } \lfloor \text{test_time} \rfloor \in [t - 5, t + 5]\}.$$

To reduce within-patient correlation and to enable patient tracking, we select at most one observation per patient in each window: for each `subject#`, we keep the record whose time is closest to t . This yields $n_{50} = 41$, $n_{100} = 38$, and $n_{150} = 39$ patient-representative observations in the three windows, with 34 patients present in all three windows and 37 patients present in both the day-50 and day-100 windows.

Severity distributions for visualization. For visualization of distribution shift and interpolations, we focus on the 2D severity vector

$$z := (\text{motor_UPDRS}, \text{total_UPDRS}) \in \mathbb{R}^2$$

and estimate its density by a Gaussian KDE. This produces smooth heatmaps for comparing the day-50, day-100, and day-150 severity distributions and for visualizing interpolated distributions.

E.0.2. Decision-focused downstream problem (care-plan selection)

Cost vectors. To evaluate decision-focused discrepancy, we embed each patient observation into a 4D cost vector

$$y = (y_{\text{ex}}, y_{\text{nurse}}, y_{\text{rest}}, y_{\text{speech}}) \in \mathbb{R}^4,$$

constructed from two severity measures and two additional covariates:

$$(\text{motor_UPDRS}, \text{total_UPDRS}, \text{age}, \text{PPE}).$$

We apply a min–max normalization on each coordinate (using the full dataset’s range), and then negate:

$$y_k := -\frac{f_k - \min(f_k)}{\max(f_k) - \min(f_k)} \in [-1, 0].$$

This normalization yields a stylized but interpretable model: larger disease burden (or higher-risk covariate values) correspond to more negative coefficients, i.e., larger marginal benefit from allocating hours to that intervention type. (Our objective is to minimize $y^\top w$, so more negative coefficients incentivize allocating more hours.)

Decisions. The decision is a weekly care plan

$$w = (h_{\text{exercise}}, h_{\text{nursing}}, h_{\text{rest}}, h_{\text{speech}}) \in \mathbb{R}^4,$$

with each coordinate interpreted as hours per week allocated to a care modality: physical exercise/physiotherapy, nursing/care coordination, sleep/rest optimization, and speech therapy.

Feasible region. We use a compact polyhedral region whose extreme points correspond to five clinically interpretable care plans (hours per week), each summing to 10 total hours:

$$w^{(1)} = (3, 3, 3, 1) \quad (\text{balanced})$$

$$w^{(2)} = (6, 2, 2, 0) \quad (\text{exercise-focused})$$

$$w^{(3)} = (2, 6, 2, 0) \quad (\text{nursing-focused})$$

$$w^{(4)} = (2, 2, 6, 0) \quad (\text{rest-focused})$$

$$w^{(5)} = (3, 3, 2, 2) \quad (\text{speech add-on}).$$

We set $S := \text{conv}\{w^{(1)}, \dots, w^{(5)}\}$. Since the downstream objective is linear, the oracle $w^*(x) \in \arg \min_{w \in S} w^\top x$ (Equation (4)) always returns an extreme point and therefore is piecewise constant, matching the structural assumptions used in our theory.

Interpretation. When y is more negative in the “exercise” coordinate (high motor severity), the optimizer tends to pick a plan with larger h_{exercise} , and similarly for nursing, rest, and speech. Operationally, $y^\top w$ can be interpreted as a negative proxy for expected symptom improvement: minimizing $y^\top w$ corresponds to selecting the care plan expected to yield the greatest benefit under the patient’s true clinical state.

E.0.3. Geometric vs decision-focused discrepancy between day 50 and day 150

Decision-blind Wasserstein distances on severity. On the 2D severity space $z = (\text{motor_UPDRS}, \text{total_UPDRS})$, the day-50 and day-150 empirical distributions are separated by $W_1 \approx 4.339$ and $W_2 \approx 5.090$. These values reflect a nontrivial shift in severity over approximately 100 days and motivate constructing intermediate distributions via interpolation.

Decision-focused distances on care-plan costs. Let $\hat{\mu}_{50}$ and $\hat{\nu}_{150}$ denote the empirical distributions of the 4D cost vectors at day 50 and day 150. Using the SPO loss ℓ_{SPO} as the transport cost (Definition 1), we compute the optimistic and robust DF distances (Definition 2) and the i.i.d. regret:

$$W_{\text{DF}}^{\text{O}}(\hat{\mu}_{50}, \hat{\nu}_{150}) \approx 0.0061, \quad R(\hat{\mu}_{50}, \hat{\nu}_{150}) \approx 0.4566, \quad W_{\text{DF}}^{\text{R}}(\hat{\mu}_{50}, \hat{\nu}_{150}) \approx 0.8605.$$

The large gap between W_{DF}^{O} and W_{DF}^{R} emphasizes that *how* the two marginals are coupled can drastically change the expected decision degradation. In particular, the very small optimistic distance indicates that there exists a coupling aligning day-50 and day-150 outcomes so that the downstream care plan remains nearly optimal on average, while the robust distance quantifies a worst-case coupling that amplifies decision degradation.

Quantity (day 50 vs day 150)	Value	Interpretation
W_1 on (motor,total)	4.3391	geometric shift in severity
W_2 on (motor,total)	5.0900	quadratic transport shift
$W_{\text{DF}}^{\text{O}}(\hat{\mu}_{50}, \hat{\nu}_{150})$	0.0061	optimistic DF distance (best-case alignment)
$R(\hat{\mu}_{50}, \hat{\nu}_{150})$	0.4566	i.i.d. regret (independent coupling)
$W_{\text{DF}}^{\text{R}}(\hat{\mu}_{50}, \hat{\nu}_{150})$	0.8605	robust DF distance (worst-case alignment)

Table 2 Geometric Wasserstein distances on the 2D severity space and decision-focused distances based on the SPO loss between day 50 and day 150 empirical distributions. The DF distances use the 4D cost vectors (motor_UPDRS, total_UPDRS, age, PPE) and the care-plan feasible region S .

E.0.4. Coupling-induced interpolations and evaluation at day 100

Interpolants. Following Section 5.2, each coupling between day 50 and day 150 induces an intermediate distribution at day 100 via the linear interpolation map $\pi_{1/2}(x, y) = (x + y)/2$. We visualize interpolated severity densities by pushing forward the coupling through $\pi_{1/2}$ and projecting onto the (motor,total) coordinates. Qualitatively, optimistic DF couplings produce interpolants that preserve decision regions, whereas robust DF couplings spread mass toward adverse regions, yielding conservative intermediate distributions.

Patient-tracked prediction task. To evaluate decision impact at the individual level, we use the 37 tracked patients present in both the day-50 and day-100 windows. For a given coupling γ between day 50 and day 150, we construct a patient-specific day-100 cost prediction by conditioning on the patient’s day-50 state:

$$\widehat{Y}_{100}(i) := \frac{1}{2} Y_{50}(i) + \frac{1}{2} \mathbb{E}_\gamma [Y_{150} \mid X_{50} = Y_{50}(i)].$$

We then evaluate the patient-level decision loss against the patient’s *true* day-100 cost vector using the SPO loss:

$$\ell_{\text{SPO}}(\widehat{Y}_{100}(i), Y_{100}(i)).$$

This evaluation isolates the impact of coupling assumptions on *downstream care-plan quality*.

Baselines. We compare decision-focused couplings against two decision-blind baselines: (i) the independent coupling $\hat{\mu}_{50} \otimes \hat{\nu}_{150}$ (no persistence), and (ii) the standard W_2 coupling minimizing squared Euclidean cost in feature space. We report mean patient-tracked SPO loss (smaller is better).

Method	Mean tracked SPO loss (50→100)
Unregularized optimistic DF coupling (DFO)	0.0167
Decision-blind W_2 coupling in 4D feature space	0.0231
Independent coupling ($\mu \otimes \nu$)	0.0945
Unregularized robust DF coupling (DFR)	0.2311
Decision-blind W_2 coupling on (motor,total) only	0.1165

Table 3 Patient-tracked evaluation at day 100: mean SPO loss incurred by decisions optimized for predicted costs

at day 100 (built from a day 50 observation and a coupling between day 50 and day 150), evaluated against the patient’s true day 100 costs. Smaller is better.

Insights: why decision-focused couplings matter. Table 3 highlights three key findings. First, the optimistic DF coupling achieves the smallest mean SPO loss (≈ 0.0167), improving upon the decision-blind W_2 coupling in the same 4D space. This demonstrates that geometric matching is not automatically aligned with downstream decision quality. Second, the independent coupling performs substantially worse (≈ 0.0945), indicating that ignoring temporal dependence can materially degrade downstream decisions. Third, the robust DF coupling yields a much larger mean loss (≈ 0.2311). This is expected: robust coupling is designed to *stress test* decision degradation under worst-case alignment rather than to forecast the most likely evolution. In preventive healthcare terms, W_{DF}^R provides a conservative upper bound on decision risk that can be used to decide whether intermediate re-measurement (here, around day 100) is warranted.

Tracked transitions vs independence. Because this dataset includes patient identifiers, we can also compute SPO loss using the *true* tracked alignment from day 50 to day 150 (matching identical `subject#`). The mean tracked SPO loss over the 38 patients observed in both windows is ≈ 0.0359 , with a median of 0. In contrast, the independent regret $R(\hat{\mu}_{50}, \hat{\nu}_{150}) \approx 0.4566$ is an order of magnitude larger. This gap empirically confirms the motivating phenomenon from Section 1.1: temporal dependence (persistence) matters, and an i.i.d. coupling can substantially overestimate decision degradation when patients evolve smoothly.

E.0.5. Entropy-regularized DF couplings and the ε trade-off

Regularized couplings. We compute the entropy-regularized optimistic and robust DF couplings from Definition 3 using a log-domain Sinkhorn algorithm, with $\varepsilon \in \{0.1, 0.2, 0.5, 1, 2, 5\}$. As ε increases, the KL penalty forces γ toward the independent coupling $\hat{\mu}_{50} \otimes \hat{\nu}_{150}$, yielding smoother couplings and more stable estimates at the cost of reduced structure.

Patient-tracked day-100 decision quality vs ε . Table 4 reports mean tracked SPO loss at day 100 for E-DFO and E-DFR couplings. Two monotone trends emerge: (i) E-DFO losses increase with ε , approaching the i.i.d. baseline, and (ii) E-DFR losses decrease with ε , also approaching the i.i.d. baseline. This behavior is consistent with the interpretation of entropy regularization as interpolating between extreme couplings and independence.

Figure 10 further visualize the distribution change as the value of ε increase.

In Figure 10, the first row shows the optimistic DF divergence with different values of ε . The shape gets further away from the true density as ε increase. The second row shows the robust DF divergence. Since the real-world case often tend to minimum tranport, the robust case is not as close to the true density as the optimistic case. ε provides a tunable bias-variance trade-off in coupling selection. Small ε yields highly structured couplings: E-DFO closely matches the

ε	0.1	0.2	0.5	1	2	5
E-DFO mean tracked SPO	0.0167	0.0167	0.0340	0.0366	0.0673	0.0785
E-DFR mean tracked SPO	0.2930	0.2537	0.2206	0.1756	0.1126	0.0960

Table 4 Effect of entropy regularization on patient-tracked decision quality at day 100. E-DFO corresponds to the entropy-regularized optimistic coupling and E-DFR to the entropy-regularized robust coupling (Definition 3). As ε increases, both regularized couplings approach the independent coupling.

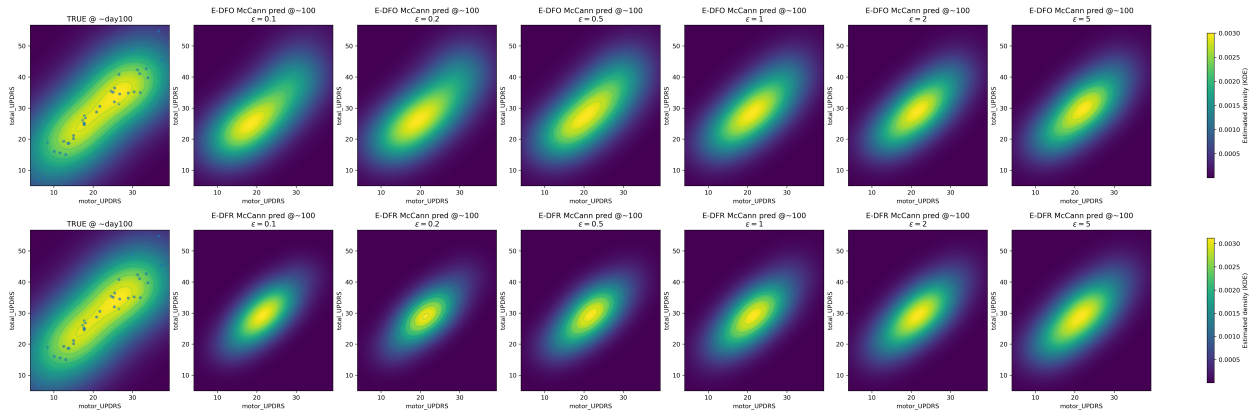


Figure 10 Optimistic and Robust DF interpolations under different values of regularization ε .

unregularized optimistic coupling and provides strong patient-specific predictions (low SPO loss), while E-DFR yields conservative, high-risk predictions suitable for stress testing. Larger ε shrinks both couplings toward independence, reducing sensitivity to sampling noise but discarding persistence information.

E.0.6. Finite-sample behavior: estimation error vs sample size

Experiment design. To empirically study estimation error, we treat the full patient-representative day-50 and day-150 samples as reference measures and repeatedly subsample n patients from each window without replacement. For each subsample, we recompute $\widehat{W}_{\text{DF}}^{\text{O}}$ and $\widehat{W}_{\text{DF}}^{\text{R}}$ and report absolute errors relative to the reference values.

Results. Table 5 reports representative results (50 trials per n). The estimation error decreases rapidly as n grows, and the robust distance exhibits larger variability, reflecting the adversarial nature of the robust coupling. Overall, the empirical trend aligns with the dimension-independent convergence behavior predicted by our theory: despite the 4D cost vector, the downstream oracle $w^*(\cdot)$ takes values in a small finite set of extreme points, so estimation depends primarily on how well the sample resolves the induced decision regions rather than on covering the ambient space.

n	$ \widehat{W}_{DF}^O - W_{DF}^O $ (mean)	(10%,90%)	$ \widehat{W}_{DF}^R - W_{DF}^R $ (mean)	(10%,90%)	trials
5	0.1527	(0.0061,0.3361)	0.2177	(0.0392,0.4935)	50
10	0.0763	(0.0239,0.1533)	0.1493	(0.0139,0.3439)	50
18	0.0286	(0.0032,0.0544)	0.0980	(0.0195,0.2134)	50
35	0.0075	(0.0009,0.0175)	0.0297	(0.0085,0.0659)	50

Table 5 Finite-sample estimation error for the optimistic and robust DF distances in the Parkinson's study. We treat the full patient-representative samples at day 50 and day 150 as the reference measures and repeatedly subsample n patients from each side (50 trials per n). Reported are the absolute errors relative to the reference values.